Zhuang, L., Zang, A. (2021): Laboratory hydraulic fracturing experiments on crystalline rock for geothermal purposes. - Earth-Science Reviews, 216, 103580.

https://doi.org/10.1016/j.earscirev.2021.103580

Laboratory hydraulic fracturing experiments on crystalline rock for geothermal purposes

Li Zhuang[a], Arno Zang[b,*]

[a] *Korea Institute of Civil Engineering and Building Technology, Goyang, Republic of Korea*
[b] *Helmholtz Centre Potsdam GFZ German Research Centre for Geosciences, Potsdam, Germany*

ARTICLE INFO

Keywords:

Hydraulic breakdown model
Enhanced geothermal system (EGS)
Injection scheme
Fracture observation
Acoustic emission monitoring
X-ray computed tomography

ABSTRACT

This article reviews laboratory experimental studies on hydraulic fracturing under triaxial and true triaxial stress conditions in crystalline rock for geothermal purposes, and places particular focus on the stimulation of Enhanced Geothermal Systems. First, parameters that influence hydraulic fracture initiation and propagation and breakdown pressure are reviewed and discussed. The parameters including micro-structure, fluid viscosity, injection rate, and fluid infiltration, and stress conditions are identified as the key controlling factors in hydraulic fracture growth in hard rock. Second, innovative injection schemes, such as cyclic and fatigue hydraulic fracturing, are reviewed because they show advantages both in fracture network creation in granite and in mitigating and controlling induced seismicity via fluid injection. Third, this review includes fracture-inspection techniques, non-destructive methods of acoustic emission (AE) monitoring and X-ray computed tomography (CT), and microscopic observations used for quantifying the efficiency of injection protocols. In addition to AE parameters, such as AE event rate and source location, we emphasize the importance of in-depth AE analysis on the failure mode and radiated seismic energy. X-ray CT and microscopic observation enable fractures in the rock volume to be quantified, and thereby lead to a better understanding the mechanism behind hydraulic fracturing. Combined measurements of AE and CT yield insights into the complex process of hydraulic fracture and permeability enhancement. The discussion section is enriched with diagrams that connect the injection rate and the resulting fluid infiltration zone and fracture process zone, granite-specific hydraulic fracturing behavior, and practical upscaling elements for potential field applications in geothermal fields.

1. Introduction

In addition to a limited volume of conventional oil and gas, a vast amount of thermal energy is stored in the earth. Hydraulic fracturing (HF) is a core technology used to extract energy sources from wellbores and is widely applied to conventional oil- and gas extraction, shale gas, enhanced geothermal system (EGS), and even supercritical geothermal system in volcanic areas (Hassebroek and Waters, 1964; Veatch Jr and Moschovidis, 1986; Breede et al., 2013; Watanabe et al., 2017a, 2017b). In addition, it has been used as a highly important tool for measuring in-situ stress within the Earth's crust (Fairhurst, 1964; Amadei and Stephansson, 1997; Zang and Stephansson, 2010) and has recently been applied to carbon storage in deep geologic formations (Zoback and Gorelick, 2012; Fu et al., 2017). In 1974, the concept of heat extraction from deep hot dry rock (HDR) was raised and demonstrated via field testing at the Fenton Hill HDR test facility (Brown and Duchane, 1999). The HDR reservoir is characterized by rock with naturally low permeability compared with traditional oil- and gas reservoirs with sedimentary formations. EGS employs stimulation treatments to enhance the permeability of HDR and to thereby extract geothermal resources. HF is an efficient way to increase rock permeability by generating fractures near the wellbore and in near-wellbore formations depending on the treatment design. The fracture is generated in a sealed section of the borehole in which overpressure initiates fracture growth (Economides and Nolte, 2000).

HF is a complex process involving interactions of

* Corresponding author at: GFZ German Research Center for Geosciences, Section 2.6 Seismic Hazard and Risk Dynamics, Telegrafenberg, 14473 Potsdam, Germany.
E-mail address: zang@gfz-potsdam.de (A. Zang).

naturally fractured rock mass with pressurized, intersecting fracture walls stimulated by various fluid-injection schemes including different flow rates. For more than half a century, a great deal of theoretical, experimental and numerical research has been implemented to better understand hydraulic fracturing behavior in various conditions and the mechanisms that lie behind this behavior (e.g., Bunger and Lecampion, 2017). Laboratory-based experimental study, in particular, has helped to provide a better understanding of HF growth behavior and to promote numerical simulation of HF. Adachi et al. (2007) analyzed different hydraulic fracturing models used for modeling HF processes and their theoretical backgrounds and also investigated a number of open questions concerning potential improvements to HF modeling. Li et al. (2015) reviewed HF in unconventional reservoirs and focused on influences of in-situ stresses, geological structures such as heterogeneities and pre-existing fractures, and numerical methods on HF modeling. Extensive reviews of the mechanics of hydraulic fractures and the fluid mechanics of HF have been provided by Detournay (2016) and Osiptsov (2017), respectively.

Although significant progress has been made in the area of reservoir geomechanics and its applications over the past two decades (Zoback, 2007), research in this field has mostly focused on petroleum reservoirs in which the range of encountered temperatures has been relatively low compared with that in geothermal settings (Ghassemi, 2012). In recent years, hydraulic fracturing in crystalline rock has become increasingly important in geothermal development, especially for EGS. In recent decades, more than 30 EGS projects have been developed in different countries, more than half of which are involved in igneous rock formations (Evans et al., 2012; Breede et al., 2013). Hard rock, such as granite and granodiorite, is coarse-grained and crystalline and is of igneous origin, being composed of quartz, feldspar, and micas as well as other accessory minerals. These types of granitic rock are frequently reported in EGS sites at a reservoir depth of up to 5 km (Cornet et al., 2007; Xie et al., 2015; Cornet, 2021). Granite porosity is usually below 1%, in contrast to most sedimentary rock, and granite formations usually have relatively low permeability compared with porous or fractured rock formations from petroleum reservoirs. Hydraulic stimulation treatment is therefore required to create fracture networks in EGS reservoirs in order to improve the hydraulic performance of rock formations with the ultimate goal of heat extraction. In general, creating fracture networks in tight rock at depth is a prerequisite for extracting heat from granite and gas from shale.

Hydraulic fracturing in hard, crystalline rock, however, is not as well understood as hydraulic fracturing in sedimentary rock for oil and gas (Zang and Stephasson, 2019). Two hydraulic stimulation mechanisms – hydrofracturing (i.e., creating new tensile fractures) and hydroshearing, (i.e., inducing slip along pre-existing fractures and faults) can be distinguished for an EGS (McClure and Horne, 2014; Gischig and Preisig, 2015; Cornet, 2021). An unavoidable by-product of growing these hydraulic fractures, however, is the generation of induced seismicity, as has been reported in enhanced oil recovery (Suckale, 2009; Davies et al., 2013), shale-gas fracking, and wastewater disposal (Warpinski et al., 2012; Bao and Eaton, 2016) as well as in harvesting deep geothermal energy (Giardini, 2009; Zang et al., 2014). Recently, innovative injection schemes have been proposed that drive fluid-filled fractures in a more controlled way, for example, by minimizing the associated seismic-energy release and maximizing permeability evolution (Zang et al., 2013, 2017, 2019). Additionally, the concept of multi-stage hydraulic fracturing has been suggested as a method of mitigating induced seismicity (Meier et al., 2015). More recently, cyclic water injection has been demonstrated in the laboratory to potentially be able to mitigate the seismic risks correlated with injection-driven shear slip of a natural fracture in granite (Ji et al., 2021). Experimental study on injection-induced shear slip on an artificial fracture plane of granitic rocks has been reported (Bauer et al., 2016; Ishibashi et al., 2018; Ji and Wu, 2018; Ye and Ghassemi, 2018; Huang et al., 2019). Rathnaweera et al. (2020) reviewed injection-induced seismicity correlated with fault activation in EGS. However, this topic, which is more closely related to injection-induced seismicity in the presence of faults, lies beyond the scope of this review article.

In this article, key factors that control hydraulic fracture nucleation and growth in crystalline rock are identified. The article highlights the background and importance of the hydraulic fracture breakdown mechanism followed by the impact of key influencing parameters, such as fluid viscosity, injection rate, and stress conditions. Second, we emphasize innovative injection schemes that have recently emerged. Third, this review includes a description of methods for destructive (microscopic observation) and non-destructive (acoustic emission and X-ray tomography) quantitative fracture analysis. Taken together, these considerations can help in upscaling innovative fluid-injection schemes for potential field applications in the framework of geothermal doublet design.

2. Background

Theoretical models enable a better understanding and classification of the physical mechanisms that lie behind certain phenomena. Accordingly, numerical models are developed to overcome limitations (i.e., to use a smaller scale compared with the field scale) in laboratory experimental study. Good experimental data provide the basis for the possible validation of theoretical models. Before providing a systematic review of laboratory-based experimental study on HF, we begin with a brief review of the theoretical background.

2.1. Hydraulic fracture models

Hydraulic fractures in the field usually have complex geometries that must be simplified for numerical simulation. Originally, two-dimensional hydraulic fracture propagation models with the simple geometry of a single fracture were used, such as the classical PKN model (Perkins and Kern, 1961) and the KGD model (Nordgren, 1972). The PKN model assumes that the fracture has an elliptical cross-section in both the horizontal and vertical directions and that the fracture height is constant independent of its length, with the height being much smaller than the length (Belyadi et al., 2019). The PKN model also assumes that the hydraulic fracturing energy applied via fluid injection would only be consumed by an energy loss from fluid flow and ignores fracture toughness. Unlike the PKN model, the KGD model assumes an elliptical horizontal cross-section and a rectangular vertical cross-section. The fracture width is constant in the vertical extension, independent of the fracture height. The PKN model corresponds to a viscosity-dominated regime, which is applicable for most hydraulic fracturing field treatments (Detournay et al., 2007). Many previous studies have discussed the use of the toughness-dominated regime and the viscosity-dominated regime for hydraulic fracturing applications (Garagash and Detournay, 2002; Bunger et al., 2005; Detournay, 2004, 2016; Detournay et al., 2007; Kovalyshen and Detournay, 2009; Lecampion et al., 2017; Li et al., 2019).

2.2. Hydraulic breakdown models

The hydraulic fracturing test was originally applied for in-situ stress measurement, as the breakdown pressure (BP) observed from the test is a function of principal stresses and rock parameters, such as tensile strength. BP corresponds to the peak injection pressure recorded during an injection test, and in most situations, it appears later than the hydraulic fracture initiation pressure (Lecampion et al., 2017; Wu et al., 2020). Various theoretical breakdown models have been proposed to predict BP and to explain fracturing behavior based on laboratory- and field experimental studies. Systematic reviews on breakdown models have been conducted by Guo et al. (1993a) and, more recently, by Sampath et al. (2018). Three of the most important models and their limitations are reviewed below. The first theoretical breakdown model (H-W), by Hubbert and Willis (1957), does not consider the influence of fluid infiltration or the injection rate because the rock is considered impermeable. Hydraulic fractures open in the direction of minimum principal stress, S_3, and grow rapidly in the plane containing the intermediate principal stress, S_2 and the maximum principal stress, S_1. In case of two-dimensional problems as shown in Fig. 1a, fractures grow in the direction of horizontal maximum stress. In this figure, the horizontal minimum stress, S_h, is equal to S_3, and the horizontal maximum stress, S_H, is equal to S_1. The model was verified by laboratory hydraulic fracturing experiments on stratified gelatin samples. Based on the model BP, P_b, is estimated as:

$$P_b = 3S_h - S_H + \sigma_t - p_0 \tag{1}$$

where σ_t is the hydraulic tensile strength and p_0 is the initial pore pressure. Ten years later, Haimson and Fairhurst (1967) introduced Biot's poroelastic parameter, which considers the infiltration of fluid around the borehole (H-F model) when analyzing stresses in rock, as shown in Fig. 1b. According to the H-F model, Eq. (1) is modified as

$$P_b = \frac{3S_h - S_H + \sigma_t - Xp_0}{2 - X}, X = \alpha\frac{1-2\upsilon}{1-\upsilon} \tag{2}$$

where α is Biot's poroelastic parameter and υ is Poisson's ratio. The Biot coefficient is suggested to be 0.46–0.72 for Grimsel granite (Selvadurai et al., 2019), 0.47 for Westerly granite (Detournay and Cheng, 1993), and 0.73 for Lac du Bonnet granite (Lau and Chandler, 2004). Some researchers argue that the effective stress theory is not appropriate for low-permeable rock, and a modified model was proposed by Schmitt and Zoback (1989). Moreover, the Biot coefficient can vary as a function of stress.

Unlike in the two previous models, Rummel and Winter (1983) introduced a hydraulic fracture model (R-W) based on the linear elastic fracture mechanics (LEFM) approach. The basic concept of the R-W model is explained in Fig. 1c. The fluid pressure in the borehole is indicated by p, the borehole radius by R, and the half-length of the assumed symmetrical bi-wing crack along the borehole wall by a. In the R-W model, the fluid pressure is applied to the borehole wall and the fluid can penetrate into the pre-existing crack that is assumed along the maximum horizontal stress. In contrast to previous models, this model can consider fluid infiltration and the borehole size effect. Based on the R-W model, BP, P_b, is calculated as:

$$P_b = \frac{1}{h_0(R,a) + h_a(R,a)}\left[\frac{K_{Ic}}{\sqrt{R}} + S_H f(R,a) + S_h g(R,a)\right] \tag{3}$$

where K_{Ic} is the fracture toughness (critical Mode I stress intensity factor). $h_0(R,a)$, $h_a(R,a)$, $f(R,a)$, and $g(R,a)$ are functions of the borehole radius and the assumed fracture length. The length of pre-existing crack around borehole is a difficult parameter to measure in the field. For Lac du Bonnet granite, $a = 4.3$ mm is assumed based on laboratory experimental results using LEFM theory (Haimson and Zhao, 1991).

2.3. Hydraulic fracturing of granitic rock

Experimental studies of HF tests have been widely carried out on various types of rock, such as sandstone, shale, granite, and even artificial rock. There are mainly two classifications of the HF test based on sample geometry.

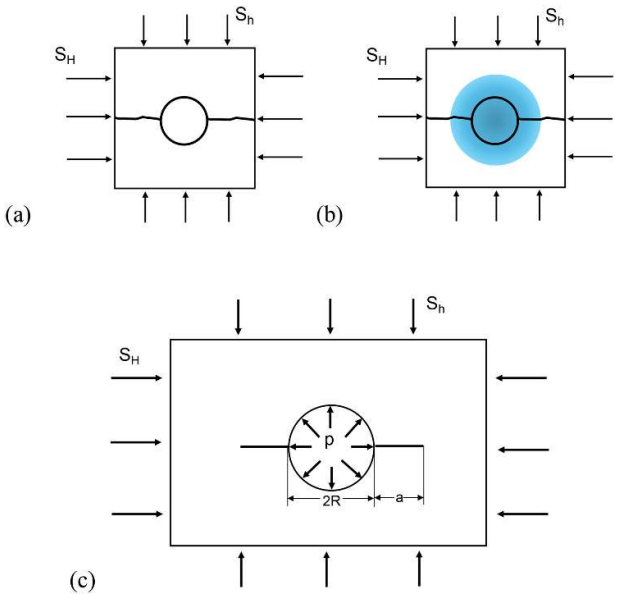

Figure 1. *Concept of three hydraulic fracture breakdown models: (a) Hubbert- Willis (H-W model), (b) Haimson-Fairhurst (H-F model), and (c) Rummel- Winter (R-W model) fracture mechanics approach; modified from Rummel (1987). S_H and S_h are the major and minor horizontal principal stresses, respectively. R is the borehole radius, and a is the half-length of the assumed symmetrical double crack along the borehole. The shadow region in (b) represents infiltration of injection fluid.*

In triaxial tests, cylindrical samples are used, and in true triaxial tests, cubic samples are used instead. The main difference between the two geometries is the condition of applied external stresses. In true triaxial HF tests, it is convenient to apply different stresses in the three directions of cubic planes to simulate the in-situ stress conditions. For conventional triaxial HF tests, confining stress (pressure vessel) and vertical stress (piston cylinder) are applied in most studies without any horizontal differential stress. Few triaxial tests have applied horizontal differential stresses in a triaxial cell using cylindrical specimens and transverse loading flat jacks (e.g., Smart, 1995; Damani et al., 2013; Patel et al., 2017). High temperatures are used with some testing equipment, particularly for geothermal studies. Zhou et al. (2020) reported the use of true triaxial hydraulic fracturing testing equipment for a 300-mm-long cubic sample under a high temperature of 200 ◦C.

Fig. 2 shows the triaxial testing system combined with acoustic emission (AE) monitoring and X-ray tomography for quantitative fracture analysis. AE sensors are installed on the triaxial cell (Fig. 2a) or directly on the samples (Fig. 2b). Fig. 2c shows triaxial HF testing in an X-ray chamber, which allows CT scanning on the pressurized sample. To improve the resolution of the CT image, the triaxial cell was made in low-density material (i.e., in engineering plastic and carbon fiber instead of in stainless steel), and the cell thickness was further reduced by selecting high-strength material. A resolution of about 105 μm can be achieved for a 50-mm-diameter granite sample using the equipment shown in Fig. 2c.

In this review, we distinguish between triaxial HF tests on cylindrical granite specimens (Table 1) and true triaxial HF tests on cubic granite specimens (Table 2). Some of the reviewed studies have an engineering background with hydraulic stimulation for EGS development. In the two tables, key parameters including granite type, specimen size, boundary conditions (applied stress, injection fluid and its viscosity, injection rate, or pressurization rate), AE monitoring, and fracture inspection methods are summarized. Experimental results and findings from these studies are discussed in the next section in terms of impact factors for hydraulic fracture initiation and growth processes. These impact factors are classified into four groups: “Sample geometry and microstructure” (Chap. 3), “Initial sample conditions” (Chap. 4), “Test conditions” (Chap. 5), and “Innovative fluid-injection schemes” (Chap. 6). The impact factors and their sub-section numbers are given in the last column of the tables. Moreover, we noted fracture inspection methods including AE monitoring, CT scanning, and others, such as microscopy and laser scan (Chap. 7). Such measurements help provide a better understanding of the HF mechanism. AE monitoring is widely applied in experimental study on HF because acoustic waves generated by initiation and a propagation of fractures can be detected by multiple AE sensors and can be further analyzed, leading to the location and failure mode of the source mechanism. This analysis is of importance when quantifying seismic-energy-release rates. Geometric fracture information can be further obtained by additional observation methods, such as CT scanning, microscopy, and laser scanning. The fracture area is required to determine the fracture surface energy as compared with the seismic energy and hydraulic energy involved in the HF process.

3. Sample geometry and microstructure

3.1. Sample geometry

As compared in Tables 1 and 2, the injection borehole size (diameter and depth) and the specimen size vary within a wide range for different studies. Reported granite specimen size has a maximum value of 1 m for cube side length (Mao et al., 2017) and a minimum of 15.9 mm for the diameter of cylindrical specimens (Solberg et al., 1980). Cubic blocks with a side length of 100–300 mm are frequently used in true triaxial HF tests. The ratio of the borehole diameter (d) and the specimen diameter (D) for cylinders or side lengths for cubic samples also varies. A few experimental cases on different granite samples were reviewed by Zhuang et al. (2018c), with the borehole diameter varying from 1.6 – 79 mm for different sizes of samples and the ratio (d/D) varying from 1/3.3 – 1/48.

Haimson and Zhao (1991) performed an extensive study on granite and limestone, and pointed out that the borehole size effect on hydraulic fracturing BP can be significant when the borehole size is relatively small in

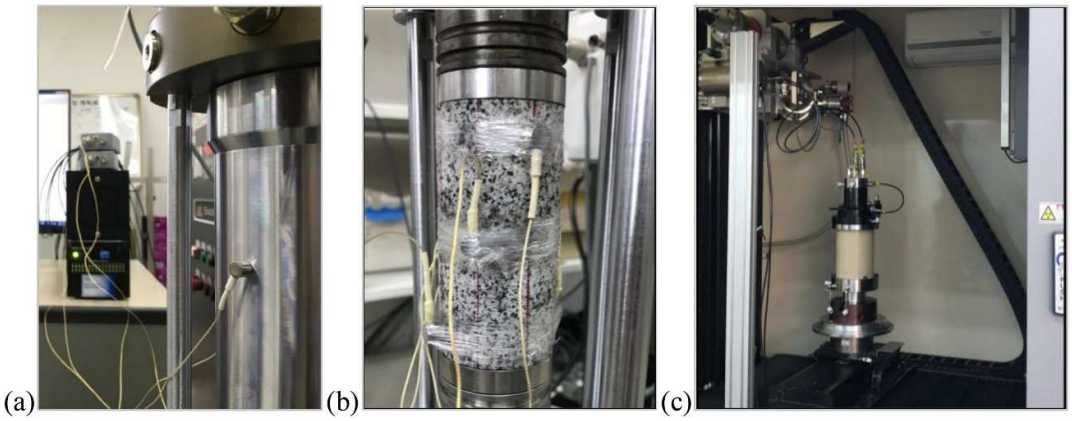

Figure 2. *Triaxial hydraulic fracturing test equipment. (a) Pressure vessel with AE sensors attached, (b) Granite core with AE sensors attached to specimen, and (c) Triaxial cell made in engineering plastic for 20-MPa confining pressure and in-situ X-ray CT scanning. In (c) cables for loading and injection purposes are tied up in bundles, resulting in a 720-degree rotation for in-situ fracture-inspection purposes.*

laboratory tests. However, when the borehole diameter is over 20 mm, BPs are essentially unaffected by borehole size. Experimental results by Morita et al. (1996) showed a clear decrease of BP of Berea sandstone when the borehole size increased from 38 mm to 100 mm.

Zhuang et al. (2018c) performed HF test on 50-mm-diameter granite core samples with four different borehole sizes of 5, 8, 12, and 14 mm. Experimental results revealed that BP decreases with increasing borehole diameter, as shown in Fig. 3. The same trend was found in sleeve fracturing tests in which the borehole had been covered by a latex membrane to prevent fluid infiltration into rock samples. These experimental values were compared with the theoretical values estimated from the LEFM model, which assumes the pre-existence of a symmetrical bi-wing crack with a half-length a (Rummel, 1987). The Pocheon granite used in the experiments has a measured fracture toughness KIc of 0.963 MPa·m0.5 and an average Brazilian tensile strength (BTS) of 6.05 MPa for the rift plane, where fractures were mainly generated (Zhuang et al., 2019a). Fig. 4a compares the theoretical predictions (assuming a=3 mm) and the experimental measurements of the BPs normalized by the BTS of the granite for both hydraulic fracturing tests and sleeve fracturing tests performed at a constant water injection rate of 100 mm3/s. The theoretical values and experimental values are in good agreement for the HF tests, whereas for the sleeve fracturing tests, the theoretical BPs were about 2 MPa higher than the experimental values (Zhuang et al., 2018c).

Similar borehole-size effects exist in the borehole breakout (BBO) test (Fig. 4b). Martin et al. (1994) compared borehole breakout tests using granite blocks with different borehole diameters ranging from 5 to 103 mm in the laboratory and from 75 mm to 3.5 m in the field. They found that the same strength-scaling law cannot be applied to laboratory and in-situ breakouts. An apparent strength-scale effect exists for boreholes less than 75 mm, and strength increases with the decreasing diameter of the borehole (Fig. 4b). The BBO test and the HF test on rock samples are similar in that fractures are usually induced near the borehole wall and then propagate. The two tests are quite different in that there is no interaction between fluid and solid in the BBO test. The failure in HF is dominated by Mode I tensile (with micro-cracks in the process zone), and the tensile strength is therefore important. The failure process in BBO can involve spalling (Mode I), shear (Mode II), and mixed- mode fracturing; the uniaxial compressive strength (UCS) of rock matters. It is widely accepted that the borehole wall strength (BWS) in the BBO test can be estimated from the UCS of rock cores, and the ratio of the BWS and UCS decreases nonlinearly with increasing borehole radius (Lin et al., 2020a). A recent true triaxial experimental study on sandstone revealed that a larger borehole tends to yield deeper and wider breakouts, and this influence should not be ignored when estimating in-situ stresses (Lin et al., 2020b).

Only very limited investigation into the influence of specimen size has been undertaken. Guo et al. (1993b) compared the HF test results of two sizes of blocks, 305x305x305 mm and 610x584x305 mm, and reported that there was no effect of specimen size on BP. Zhuang et al. (2018c) investigated the HF behavior of granite samples with a diameter of 50 mm and three different heights of 50, 70, and 100 mm. Specimen height exerted nearly no influence on BP, regardless of the relatively low or high injection rate.

3.2. Grain size

Grain size has great influence on the initiation and propagation of brittle fractures. Eberhardt et al. (1999) performed uniaxial compression tests on three types of granite with average grain size of about 1 mm, 3 mm, and 20 mm. They found that longer grain boundary cracks and longer intergranular cracks are formed when testing rock with larger grain size. These longer cracks promoted the degradation of material strength once they had begun to

Table 1
Triaxial hydraulic fracturing tests on granite cylinders.

Reference	Testing rock (mean grain size)	Specimen and borehole size (mm)	Applied stress σ_c, σ_v (MPa)	Injection fluid, viscosity (mPa.s)	Injection rate (mm3/s)	AE monitoring and fracture observation	Impact factor (section)
Solberg et al. (1977)	Westerly granite	D 25.4, H 63.5, d 2.5	100, 200~790	No. 15 Shell Tellus oil, 20~90	3.3E-3~3.3	-	Stress state (5.3)
Solberg et al. (1980)	Westerly granite	D 15.9, H 38.1, d 1.6 D 76.2, H 190.5, d 1.6	100, 200~400 100, 520	Water	0.33~70.4	AE (7 transducers)	Rock temperature (4.1) Injection rate (5.2) Stress state (5.3)
Haimson and Zhao (1991)	Lac du Bonnet granite	d 3.2~50.8d/D 1:4 ~ 1:8	0, unknown	Water, Light oil	5 (Pressurization rate: 0.03~10 MPa/s)	AE (one sensor)	Sample geometry (3.1) Pressurization rate (5.2)
Schmitt and Zoback (1992)	Westerly granite	D 42.8, H 110~150, d 12.8	2~16.1, unknown	Kerosene (viscosity slightly higher than water)	Pressurization rate 0.07~5.25 MPa/s	AE	Pressurization rate (5.2) Stress state (5.3)
Schmitt and Zoback (1993)	Westerly granite	D 42.8, H 110~150, d 12.8	2~60, unknown	Kerosene (viscosity slightly higher than water)	Pressurization rate 0.05, 0.6, 2.0 MPa/s	–	Sample saturation (4.2) Pressurization rate (5.2) Stress state (5.3)
Goodfellow et al. (2013)	Westerly granite (0.75 mm)	D 50, H 125, d 6.35 Half drilled	5, 120	Distilled water, 1	3.33, 8.33	AE (18 sensors)	Injection rate (5.2)
Diaz et al. (2016a)	Pocheon granite (0.91~1.01 mm)	D 50, H 100, d 8 Fully drilled	(0, 5), 25	Tap water	25, 50 (Pressurization rate control 0.1 MPa/s)	CT scanning	Rock anisotropy (3.3) Injection rate (5.2)
Goodfellow et al. (2016)	Westerly granite (0.75 mm)	D 50, H 125, d 10 Half drilled	12~30, 10	Distilled water, 1	4.2~66.7	AE (19 sensors & ultrasonic velocities sensors)	Stress state (5.3)
He et al., 2016	Granite	D 50, H 90, d 8 Half drilled	20, 25	water	200 mm3/s	CT scanning	Rock anisotropy (3.3)
Jung et al. (2016)	Pocheon granite (0.91~1.01 mm)	D 50, H 100, d 8 Fully drilled	0, 25	Tap water Oil, 80, 122 and 152	1~100	CT scanning	Fluid viscosity (5.1) Injection rate (5.2)
Zhuang et al. (2016)	Pocheon granite (0.91~1.01 mm)	D 50, H 100, d 8 Fully drilled	5, 25	Tap water	Pressurization rate control 0.1 MPa/s	CT scanning	Rock anisotropy (3.3) Cyclic hydraulic fracturing (6.1)
Watanabe et al. (2017a, 2017b)	Inada granite	D 30, H 25, d 1.5 Half drilled	40, 90	Water at 40 MPa: 143 (200◦C), 77 (360◦C), 39 (450◦C)	50	CT scanning	Rock temperature (4.1)
Kumari et al. (2018)	Strathbogie granite (0.3-1.5 mm) Harcourt granite (0.3-2.5 mm)	D 22.5, H 45, d 3 Half drilled	Confining pressure 0~60	Water	83.3	CT scanning	Rock temperature (4.1) Stress state (5.3)
Stephansson et al. (2019)	Äspö diorite, Fine-grained granite, Ävrö granodiorite	D 96, H 200, d 6 Half drilled	12.1, 8.5	Water	Pressurization rate 0.1 MPa/s	-	Fatigue hydraulic fracturing (6.2)
Zhuang et al. (2018c)	Pocheon granite (0.91~1.01 mm)	D 50, H 100, d 5, 8, 12, 14 Fully drilled	0, 25	Tap water	5, 25, 50, 100	CT scanning	Sample geometry (3.1) Injection rate (5.2)
Diaz et al. (2018b); Zang et al. (2019)	Pocheon granite (0.91~1.01 mm)	D 50, H 100, d 5 Fully drilled	0, 25	Tap water	50	AE (6 sensors) CT scanning	Cyclic hydraulic fracturing (6.1)
Zhuang et al. (2019a)	Pocheon granite (0.91~1.01 mm)	D 50, H 100, d 8 Fully drilled	0, 25	Tap water	1~100	CT scanning	Injection rate (5.2) Pre-existing flaws (4.3)
Zhuang et al. (2019a)	Pocheon granite (0.91~1.01 mm)	D 50, H 100, d 8 Fully drilled	0, 25	Tap water	100	AE (2 sensors) CT scanning	Cyclic hydraulic fracturing (6.1)
Zhou et al. (2018)	Shandong grey granite	D 200, H 400, d 18 Half drilled	25, 25	Water	Instantaneous value 0-40,000	-	Rock temperature (4.1)
Zhuang et al. (2020a)	Pocheon granite (0.91~1.01 mm)	D 50, H 100, d 5 Fully drilled	0, 10	Tap water	100	AE (6 sensors) CT scanning	Sample saturation (4.2) Pre-existing flaws (4.3)

Note) D: diameter of cylindrical specimen, H: height of specimen, d: diameter of borehole, σ_c: confining stress, σ_v: vertical stress. Viscosities of fracturing fluids and number of AE sensors were not reported in several studies. Most studies applied injection rate control while a few exceptions applied pressurization rate control.

coalesce and interact. The grain-boundary effect (or Hall-Petch strengthening) indicates an increase in the yield strength of a polycrystalline material as its average grain size decreases (Cordero et al., 2016). This effect is well-known in metal but also applies to rock. Ishida et al. (2000) investigated the HF behavior of four different types of granitic rock with small to large grain sizes at given maximum and minimum horizontal stresses of 12 MPa and 6 MPa, respectively. Experimental results revealed that horizontal fracture planes perpendicular to the borehole direction were created in the two rock samples with large mean grain sizes of 0.88 mm and 1.12 mm, while vertical fracture planes parallel to the borehole direction were created in the two types of granitic rock with small mean grain sizes of 0.51 mm and 0.68 mm. The dominant micro-fracturing mechanism became tensile rather than shear with decreasing grain size. The authors further noted that the different hydraulic fracturing behavior with different grain sizes could eventually be attributed to the pre-existing defects or microcracks and deduced that the shear type fracture is expected to occur mainly through the connection of tips of pre-existing defects.

The schematic diagram in Fig. 5 summarizes the two cases of small-and large-grain granitic rock under the same test conditions assuming that there are defects such as the pre-existing microcracks in rock specimens. The mineral grains themselves in granite such as quartz and feldspar are known to have higher tensile strength than the bonding strength of the interface between minerals (Savanick and Johnson, 1974). Pre-existing defects reduce the strength. Hydraulic fracture initiates near the borehole wall due to its maximum tensile hub stress, and intergranular or intragranular tensile cracks are generated and form a main fracture. In the small-grain assembly, tensile cracks can form in a process zone through mineral breakage by intra- or intergranular cracking (Fig. 5a), which is kidney-shaped for Mode I fractures. In the large-grain assembly, more energy is required to split large mineral grains compared with the grain boundary, and more hydro-shears along grain boundaries or pre-existing microcracks are thus expected to be generated as they require less energy (Fig. 5b). The large grain size

Table 2
True triaxial HF tests on cubic granite samples.

Reference	Testing rock	Specimen size and borehole diameter (mm)	In-situ stresses (MPa) σ_h - σ_H - σ_v or σ_1 - σ_2 - σ_3	Injection fluid, viscosity (mPa.s)	Injection rate (mm3/s)	AE monitoring and fracture observation	Impact factor (section)
Zhao et al. (1996)	Lac du Bonnet granite	127 × 127 × 175 d 20	(10, 20, 30)-(20~60) -(40, 50)	Water	10, 120, 400	AE	Injection rate (5.2) Stress state (5.3)
Ishida et al. (1997)	Kurokami-jima granite	190 × 190 × 190 d 20	3-6-0	Water	166.7	AE (12 sensors)	Injection rate (5.2)
Ishida et al. (2000) Ishida (2001)	Granites and granodiorites with average grain size: 0.51, 0.68, 0.88, 1.12 mm	200 × 200 × 200 d 10	6-12-0	Water, 1	73.3~81.7	AE (9 sensors)	Grain size (3.2)
Takehara et al. (2003)	Granite	200 × 200 × 200 d 10	8-8-8	Water	166.7, 250, 500	AE (8 sensors)	Injection rate (5.2)
Ishida et al. (2004)	Kurokami-jima granite	190 × 190 × 190 d 20	3-6-0	Water, 1 Oil, 80	166.7	AE (12 sensors) Pre-existing flaws (4.3)	
Frash (2014) Frash et al. (2015)	Colorado rose red granite	300 × 300 × 300 300 × 300 × 240 d 3.2	4.1-8.3-12.5	Tap water, 0.354~0.942 Valvoline oil, 22.6~323 Epoxy, 8E3~4E4	0.17, 0.83, 1.67	AE (6 sensors)	Temperature (4.1) Fluid viscosity (5.1) Injection rate (5.2)
Ishida et al. (2012)	Kurokami-jima granite	170 × 170 × 170 d 20	1-1-1	SC-CO2, 0.05~0.1 Liquid CO2, 0.5~1	500	AE (16 sensors)	Fluid viscosity (5.1)
Kizaki et al. (2013)	Inada granite	150 × 150 × 150 d 20	3-5-1	Water, SC-CO2	160, 833, 2500	Red tracer	Fluid viscosity (5.1) Injection rate (5.2)
Chen et al. (2015) Ishida et al. (2016)	Kurokami-jima granite	170 × 170 × 170 d 20	3-6-4	Water, Oil, L-CO2, SC-CO2, 0.05~336.6	166.7	AE (16 sensors) & microscopy	Fluid viscosity (5.1)
Lu et al. (2015) Lu et al. (2020)	Coldspring Charcoal granite	150 × 150 × 150 d 12.5	0.1-0.1-0.1	Water, 1 Glycerin, 1080	3333.3	–	Fluid viscosity (5.1)
Hu et al. (2016, 2017, 2019)	Sierra White granite	330 × 330 × 330 Injection well *d* 20 Production well *d* 10	3.79-3.10-2.62 4.83-8.27-3.79 6.89-10.34-3.45	water	33.3	AE (16 sensors) & laser scanner	Pre-existing flaws (4.3) Stress state (5.3)
Mao et al. (2017)	Luhui granite	1000 × 1000 x1000 d 79	2-(5~8)-8	Water, 1	166.7	AE (12 sensors)	Pre-existing flaws (4.3) Stress state (5.3)
Zhuang et al. (2018a) Diaz et al. (2018a)	Pocheon granite	50 × 50 × 50 d 5	10-20-20	Tap water	200	AE (8 sensors) CT scanning	Pre-existing flaws (4.3) Cyclic hydraulic fracturing (6.1)
Diaz et al. (2018c) Zhuang et al. (2020c)	Pocheon granite	100 × 100 × 100 d 5	3-6-4	Tap water	10-400 * Pressurization rate 0.3 MPa/s	AE (8 sensors) CT scanning & microscopy	Cyclic and fatigue hydraulic fracturing (6.1 & 6.2)
Gonçalves Silva and Einstein (2018)	Barre granite	152 × 76 × 25	Vertical load: 0 and 5	Distilled water	0.5 MPa/s	AE (8 sensors) & microscopy	Pre-existing flaws (4.3)
Hampton et al. (2018)	Dakota granite	150 × 150 × 250 d 10	13.79-6.89-3.45	Gear oil	1.67	AE (11 sensors) CT scanning	Test conditions (5)
Xing et al. (2019)	Shandong granite	300 × 300 × 300 d 25	0.1-0.1-0.1 10-25-30	CaCl2 solution at -20◦C, 1	33.3	AE (8 sensors)	Rock temperature (4.1) Stress state (5.3)
Zhang et al. (2019b)	Rizhao granite	100 × 100 × 120 d 14	5-7.5-10	Distilled water	Not reported	Red tracer Rock temperature (4.1)	
Zhou et al. (2020)	Gonghe granite outcrop	300 × 300 × 300	Horizontal differential stress: 10 and 20	Water, 1	1.9, 3.8, 10 m3/ min (scale-up)	Green tracer	Pre-existing flaws (4.3) Injection rate (5.2) Stress state (5.3)

Note) σ_h: minimum horizontal stress, σ_H: maximum horizontal stress, σ_v: vertical stress, d: diameter of borehole. Viscosities of fracturing fluids and number of AE sensors were not reported in several studies.

compared with the borehole radius does not allow for a proper Mode I fracture process zone to be developed. Instead, segmented boundary cracking occurs and consumes most of the energy in localized shear failure at larger grains. In geothermal terminology, this is referred to as localized hydro-shear failure.

3.3. Rock anisotropy

Rock anisotropy, such as in shale, sandstone, and cemented materials, has great influence on hydraulic fracturing behavior (Stoeckhert et al., 2015; Zou et al., 2016; Huang and Liu, 2017; He et al., 2016). Most granite has clear anisotropy, though it is not as significant as compared with sedimentary rock (Peng and Johnson, 1972; Duevel and Haimson, 1997). In anisotropic granite, usually three mutually perpendicular weak planes or cleavages exist with different densities of existing microcracks and mineral distributions, which are called rift, grain, and hardway (Osborne, 1935; Douglass and Voight, 1969). In quarrying, the three cleavage planes are identified based on how easily they split the rock. Rift is the direction of easiest splitting (smallest tensile strength), and the grain is next to the rift. The hardway is the plane of most difficult splitting (largest tensile strength) among the three planes. Fig. 6 shows directions of rift, grain and hardway in a granite quarry in the Pocheon area of South Korea. This Pocheon granite has been frequently used in hydraulic fracturing experiments, which are introduced below. Differences in physical and mechanical properties have been reported, including tensile and compressive strength, fracture toughness, hydraulic conductivity, and the roughness of the fracture plane, all of which correspond to different testing planes (Zhuang et al., 2016, 2019a; Diaz et al., 2016a). The influence of the anisotropy of granite on hydraulic fracturing behavior has been reported by Chen et al. (2015), Diaz et al. (2016b), and Zhuang et al. (2019a). However, some research has considered the granite anisotropy at a core-scale to be non-significant for the field application because the scale of microcracks is not comparable to that of natural joints

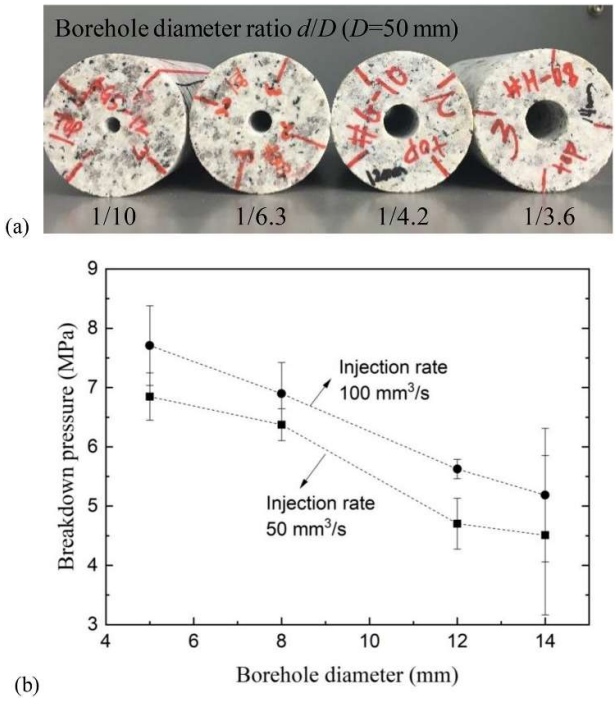

Figure 3. *Laboratory hydraulic fracturing experiments on the borehole size effect. (a) Specimen geometry of Pocheon granite and (b) BP versus borehole diameter for two injection rates (modified from Zhuang et al., 2018c).*

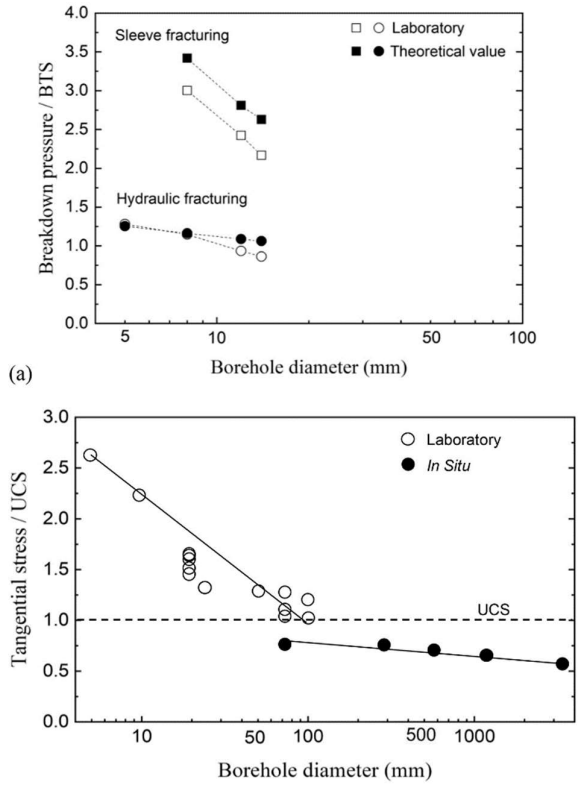

Figure 4. *Borehole size effect for (a) hydraulic fracturing and (b) borehole breakout formation (modified from Zhuang et al., 2018c; Martin et al., 1994). In (a), BP is normalized to the Brazilian tensile strength of rock. In (b), the tangential stress at the borehole wall is normalized to the uniaxial compressive strength of rock. In both diagrams, the borehole diameter is plotted logarithmically to account for the stress concentration at the borehole wall.*

and fractures (Zoback and Byerlee, 1975). Duevel and Haimson (1997) noted that the pink Lac du Bonnet granite is quasi-isotropic in compression despite the fact that its tensile strength and tensile modulus show stronger anisotropy.

Foliation is another reason for the anisotropy of granitic rock. A typical case was reported for granite at the Grimsel site in which the orientation of the fracture initiation deviated from the direction of the maximum principal stress due to the influence of foliation (Dutler et al., 2019). Similarly, natural weak planes, such as veins in granite samples, will affect hydraulic fracture initiation or propagation (Zhou et al., 2020). Theoretically, hydraulic fractures propagate parallel to the maximum horizontal stress. When the maximum principal stress is parallel to the foliation (the preferred mineral orientation), the hydraulic fracture propagates along the foliation and is relatively straight (Fig. 7a); when the orientation of the maximum principal stress is perpendicular to the foliation, the hydraulic fracture propagation deviates from the direction of maximum principal stress when meeting weak local areas (grain boundaries), and fracture thus becomes more tortuous (Fig. 7b).

4. Initial sample conditions

4.1. Rock temperature

Mechanical, physical, and thermal properties of granitic rock are largely influenced by temperature, particularly at high temperatures close to the melting point of rock (Heuze, 1983). The influence of temperature has been frequently considered in granitic rock for the purpose of EGS stimulation (Solberg et al., 1980; Frash, 2014; Frash et al., 2015; Ghassemi, 2012; Hu et al., 2016, 2017; Zhang et al., 2019a; Xing et al., 2019). Solberg et al. (1980) compared the HF behavior of granite samples at low and high temperatures of 25°C and 200°C, respectively. They concluded that temperature exerted a minor effect on the HF mechanism and could not demonstrate the occurrence of thermal fracturing. Injected fluid has relatively low viscosity at a high temperature, and this could have reduced the pressure gradient near the borehole. Xing et al. (2019) also noted that shear cracks were reduced by 6–12% when the testing temperature was increased from 20 ◦C to 120°C. Zhou et al. (2018) conducted hydraulic fracturing tests on granite at different temperature conditions of 20, 100, 200, 300, and 400°C. A recent study on EGS development in Gonghe Basin investigated the influence of temperature through laboratory true triaxial hydraulic fracturing tests (Zhou et al., 2020). The HF tests were conducted on cubic samples with a side length of 300 mm from a granite outcrop at a temperature of 200°C. Li et al. (2020a) quantified the thermal effects on physical properties and fracture initiation of Laizhou granite during hydraulic fracturing. Through scanning electron microscopy

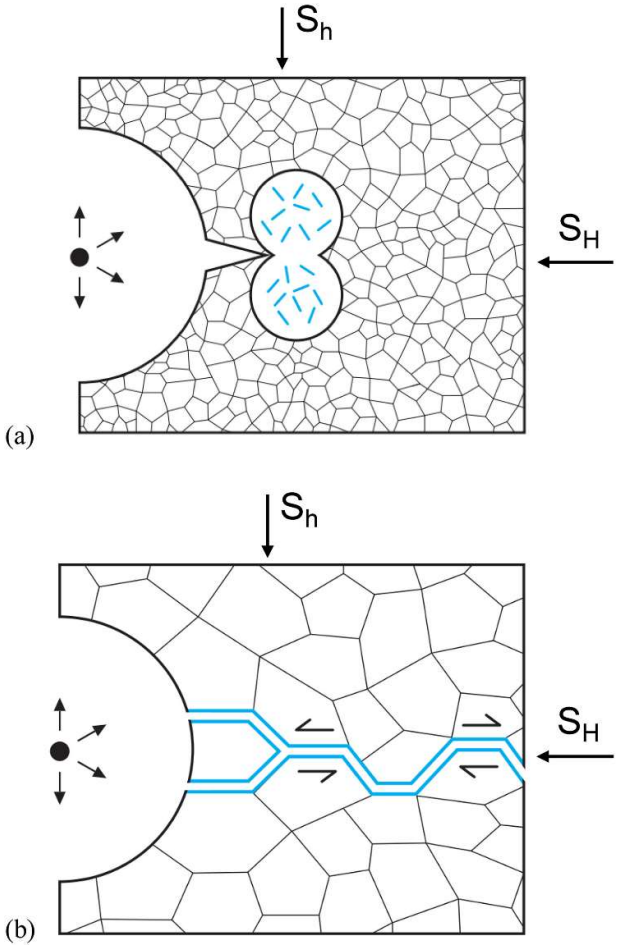

Figure 5. *Schematic representation of hydraulic fracturing in (a) small-grain granitic rock and (b) large-grain granitic rock with respect to borehole size. In (a), a process zone ahead of the hydraulic fracture develops with chiefly Mode I cracks inside. In (b), grain boundary hydro-shear (Mode II) develops since larger grains prevent the proper evolution of the process zone at the borehole scale. Blue indicates the formation of new, fluid-filled cracks from the hydraulic fracture.*

analysis, isolated fractures grew and coalesced with a significant increase in porosity and gas permeability at a threshold temperature of 300°C during rapid cooling. Above 300°C, BP was reduced significantly due to strength weakening. For example, a maximum reduction of 42% occurred when comparing results from tests with temperature 25°C and 500°C, respectively. This process is associated with thermal cracking, fluid leak-off, and a decrease in the buildup rate of injection pressure. Based on AE hypocenter analysis, shear cracks became dominant compared with tensile cracks when the temperature was above 300°C (Li et al., 2020a).

The experimental results described above revealed that BP decreases with increasing temperature and that the temperature influence is much more significant when the temperature exceeds 200°C. This finding has several explanations: First, tensile strength decreases at high temperatures (Yin et al., 2015). Second, tensile stress caused by thermal shock, which is flow-rate dependent, changes the stress distribution near the borehole and accelerates crack initiation (Shen et al., 2013). Theoretical equations of the thermally induced stresses at the borehole wall, which are dependent on rock properties and temperature difference, were provided by Stephens and Voight (1982). As a result, Eq. (1) can be modified by adding a new item of thermal stress.

Thermal stimulation, in which cold water compared with the temperature of the rock mass was injected, has been reported in EGS development (Bradford et al., 2014). Stresses in rock formation change due to large temperature differences between cold water and the reservoir, thereby leading to the stimulation of natural fracture networks or to the initiation of new fractures. The initiation and growth of thermal fractures could occur near the wellbore. Temperature differences between reservoir rock and fluids and injected fluids can complicate the interpretation of field injection test results in geothermal reservoirs (Ghassemi, 2012).

Watanabe et al. (2017a, 2017b) investigated the HF behavior of granite under high temperatures of 200°C, 360°C and 450°C at an initial effective confining pressure of 40 MPa. Permeability enhancement was confirmed at all testing conditions, ranging from subcritical-brittle to supercritical-ductile (supercritical water conditions: temperature and pressure are in excess of 374°C and 22.1 MPa, respectively). The follow-up experimental study revealed that cloud-fracture networks were generated during water stimulation at temperatures above 400°C (Watanabe et al., 2019). These findings indicate the potential of exploring supercritical geothermal energy in volcanic area.

4.2. Sample saturation

Geothermal reservoirs can differ in water content depending on whether they target hot dry rock or hydrothermal resources. The same geothermal reservoir can be subject to different degrees of saturation because hydraulic stimulation is repeatedly treated. In addition, cracks around the borehole are induced in granite formations due to accompanying stress release during drilling and to temperature differences between injected cold water and hot rock. These induced cracks and pre-existing

Figure 6. *A granite quarry in the Pocheon area of South Korea. The directions of rift-, grain- and hardway planes are indicated by arrows.*

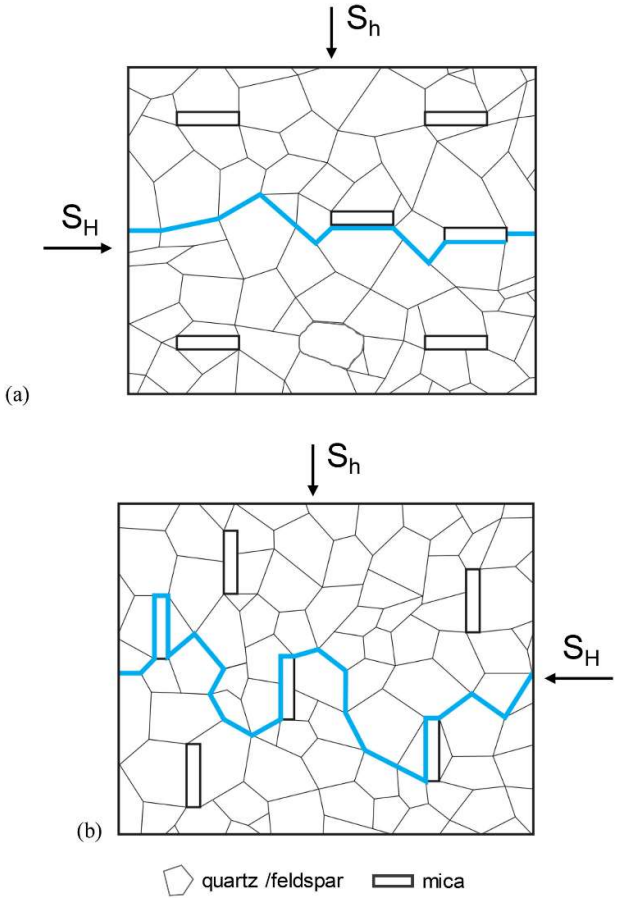

Figure 7. *Schematic representation of hydraulic fracture propagation in rock with foliation. Maximum stress (S_H) orientation is aligned (a) parallel, and (b) perpendicular to the foliation. Blue indicates the path of the hydraulic fracture in the grain aggregate. The path perpendicular to foliation shows higher tortuosity.*

discontinuities in naturally fractured reservoirs are likely partially or fully saturated by drilling fluid or injection fluid during stimulation. Experimental studies on the HF of granite have reported that the degree of saturation of initially dry specimens varies with the injection rate, which accordingly affects the rock breakdown (Zhuang et al., 2019a).

The initial state of saturation of the rock sample should be considered in HF tests combined with AE monitoring because water saturation strongly influences *P*-wave velocity, which is used for locating AE events. An increase in the P-wave velocity of granite with water saturation was reported to be 30% or more (Kahraman, 2007; Zhuang et al., 2020b). Water content is known to exert very limited influence on either the short-term compressive strength or the tensile strength of unweathered granite (Lajtai et al., 1987; Hashiba and Fukui, 2015). Zhuang et al. (2020a) found that water saturation has little influence on the magnitude of BP but accelerates fracture initiation in both mechanical and hydraulic fracturing of granite. Based on CT measurements, larger fracture areas were generated by hydraulic fracturing in the initially saturated specimens than in initially dry specimens. This finding is further supported by AE monitoring results, which revealed that the maximum AE hit rate near breakdown doubles in saturated cores as compared with in dry rock (Zhuang et al., 2020a).

4.3. Pre-existing flaws

Discontinuities in rock can have a wide range of scales, from mm to km, including microcracks at the mineral scale, cracks or fractures at the core scale, and joints or faults at the field scale. Microcracks are very frequent in crystalline rock, such as granite. Laboratory-based experimental studies have shown that microcracks in granite influence both rock strength and permeability and therefore also HF behavior (Diaz et al., 2016b; Zhuang et al., 2019a, 2019b). However, some research has revealed that the influence of microcracks in granite observed in the laboratory is not comparable with that exerted by joints or faults at the field scale (Zoback and Byerlee, 1975; Duevel and Haimson, 1997). For EGS study, it is critical to consider pre-existing fractures in laboratory experiments because the mechanism of shear stimulation that occurs through induced slip of pre-existing fractures is most often assumed in EGS stimulation (McClure and Horne, 2014). Natural fractures in rock, such as joints and faults, have a major and perhaps dominating impact on the success of EGS through their effects on flow, heat extraction and induced seismicity (Ghassemi, 2012). Moreover, the interaction of natural fractures with hydraulic fractures will change the overall mode of failure (i.e., mixed-mode failure).

For a laboratory-scale HF test, discontinuities are usually considered at the core scale, and could be either natural or artificial. Even though few experiments have been performed on rock samples with natural fractures (Blanton, 1982, 1986; Cheng et al., 2015; Zhou et al., 2020), most experiments have been performed on samples with artificial fractures. Artificial pre-existing cracks or fractures are made by creating notches near the borehole (Medlin and Masse, 1976; Groenenboom and van Dam, 2000; Pater et al., 2001; Cacas, 2005), by using a pre-fractured rock sample (Stanchits et al., 2012; Bai et al., 2016), or by creating artificial discontinuities in cement samples (Guo et al., 1993b, 1993c; Cacas, 2005; Zhou et al., 2018; Zhou et al., 2010; Fan and Zhang, 2014; Sarmadivaleh and Rasouli, 2015; Dehghan et al., 2016; Frash et al., 2016; Huang and Liu, 2017). Zhou et al. (2020) conducted laboratory hydraulic fracturing tests on cubic granite samples with a side length of 300 mm under true triaxial stress conditions. Most of the samples contained natural fractures and were mined from the outcrop of Gonghe Basin, where an EGS project was underway. Laboratory experimental study has shown that the main hydraulic fracture was generated parallel to the direction of the maximum horizontal stress and connects the pre-existing natural fracture plane (Fig. 8).

Injection-induced fracture propagation and coalescence in granite cores containing a single pre-cut fracture

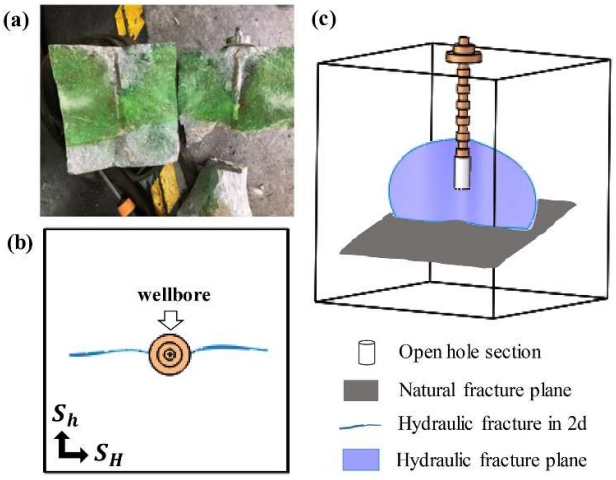

Figure 8. *Interaction of a natural fracture and a hydraulic fracture created in a sample of cubic granite with a 300-mm side length under true triaxial stresses (modified from Zhou et al., 2020). In (a), the hydraulic fracture is filled with green dye. In (b), the hydraulic fracture (blue) is parallel to the horizontal maximum stress of S_H. In the spatial view (c), the interaction of the hydraulic fracture (blue) with an inclined pre-existing natural fracture (grey) is shown.*

or double pre-cut fractures created by water jet have been investigated (Ye and Ghassemi, 2018, 2019; Gonçalves Silva and Einstein, 2018; Xiong et al., 2021). Ye and Ghassemi (2019) conducted an experimental study on Sierra White granite and reported that pre-existing fractures can be propagated in tensile, shear, and/or mixed mode at injection pressures below the minimum principal stress. A fracture network and a dominant flow path can be formed by the coalescence of the newly propagated cracks and pre-existing fractures, resulting in remarkable enhancement of permeability/fluid flow. These experimental findings indicate the potential of the concept of hydro-shearing for pre-existing fractures in a naturally-fractured rock formation. Fluid pressure distribution in pre-existing fractures strongly affects hydro-shearing. This effect was addressed in an experimental study, recently (Ji et al., 2020).

Natural fractures (NFs) exert significant influence on created hydraulic fractures (HFs). The interaction process between NFs and HFs is highly complex, and multiple scenarios of fracture propagation have been reported, including arresting, crossing, and branching (Yew and Weng, 2015; Fatahi et al., 2017). The interaction between NFs and HFs remains a challenging topic for both experimental and numerical research (Yoon et al., 2014, 2015a, 2015b; Zhang et al., 2019b).

5. Test conditions

Rock strength and deformation measurements are always dependent on test conditions, such as the loading rate and applied external stresses. For hydraulic fracturing of rock in laboratory experiments, injection fluid in either a liquid or gaseous state is another important factor that should be taken into consideration in addition to the loading rate and external stress.

5.1. Fluid viscosity

In field application, various fluids can be used and have been applied for hydraulic fracturing. Gandossi (2013) summarized dozens of mixed fluids that are mainly used for shale-gas production. In the laboratory, a variety of injection fluids have been tested in experimental studies, the most common being water, oil, mud, gum, CO2 (liquid, super-critical), and gas (CO2, N2, etc.). Their viscosities vary in the range of between 1E-2 and 1E6 mPa.s. Experimental results show that the viscosity of injection fluid has a significant influence on the HF of granite (Ishida et al., 2004, 2012; Chen et al., 2015; Jung et al., 2016) as well as other type of rock (Chitrala et al., 2012; Fallahzadeh et al., 2017). Ishida et al. (2012, 2016) compared four different fluids of super-critical and liquid CO2, water, and viscous oil with a low to high viscosity of 0.051–336.6 mPa.s and confirmed that BP increases, while the tortuosity of fractures decreases with increasing viscosity. Moreover, it has been noted that the failure mechanism could be different for different injection fluids (Ishida et al., 2004; Shimizu et al., 2011; Ishida et al., 2012). Low-viscosity fluid such as SC-CO2 induces shear-dominant fractures (Mode II), while high-viscosity fluid induces tensile-dominant fractures (Mode I). SC-CO2 can induce more widely and complexly extending fractures than water and oil, which are relatively higher-viscosity fluids (Ishida et al., 2004, 2012).

For a given rock type, a high-viscosity fluid has a smaller infiltration rate compared with low-viscosity fluids, even at the same injection rate. As a result, a rock sample can be fractured at different BPs. Jung et al. (2016) compared the total volume of injection fluid infiltrated into granite samples using water and various oil-based fluids (80, 122, and 152 mPa.s) at the same constant injection rate. The measured results show that the total amount of oil infiltration is approximately half that of water infiltration. BPs by oil fracturing are about two times those by water fracturing, which could be explained by the different hydraulic fracturing behavior within viscosity-dominated and toughness-dominated regimes, as introduced in Section 2.1 and further discussed in Section 8.1.

Fracture properties are also influenced by the viscosity of the injected fluid. Tortuosity, roughness, and fractal dimension are used to evaluate the geometric properties of induced fractures (Ishida et al., 2012; Chen et al., 2015; Diaz et al., 2016b). High-viscosity fluids tend to produce fractures with smaller tortuosity, despite the fact that this tortuosity is also influenced by minerals and other factors, such as microcracks. Ishida et al. (2012) reported higher average fractal dimensions of fractures induced by super-critical CO_2 (2.42) than of those induced by liquid CO_2 (1.63), with higher fractal dimensions indicating that fractures extend three-dimensionally and with more secondary branches rather than along a flat plane. These

findings are highly meaningful as the goal of field applications in EGS is to create more-widely cloud-shaped fracture networks and thus to enhance permeability and enlarge the heat-extraction area.

5.2. Injection and pressurization rate

Most HF experiments have been performed under injection rate control, largely because fluid injection in the field is usually controlled by injection rate or injection volume. The terms of "flow rate" or "pumping rate" are also used in some studies instead of "injection rate". The injection rate and pressurization rate correlate with each other, though the relationship between the two may not be always linear. Extensive experimental studies have reported that BP increases with increasing injection rates for various types of rock with either low or high permeability (Haimson and Fairhurst, 1969; Zoback et al., 1977; Solberg et al., 1977, 1980; Guo et al., 1993b; Jung et al., 2016; Ha et al., 2017; Zhuang et al., 2019a). The pressurization rate has been argued to influence the BP depending on whether the rock is permeable (see Chap. 2.2, and Zoback et al., 1977; Detournay and Cheng, 1992; Garagash and Detournay, 1996). Zoback et al. (1977) reported that BPs for permeable Weber and Ruhr sandstones increase with pressurization rate. The authors further noted that, in pressurization-rate-controlled tests, the BP was found to be rate-dependent, whereas in flow-rate-controlled experiments, the BP was essentially equal to the fracture initiation pressure and was rate-independent. Experimental results reported by Schmitt and Zoback (1992, 1993) reveal that borehole pressure at fracture initiation in Westerly granite increases with increasing pressurization rates.

The effects of the injection rate or pressurization rate are correlated with the infiltration of injected fluid into rock samples during injection. The infiltration is largely influenced by fluid viscosity and discontinuities in the rock sample. Pioneering experimental and theoretical work deals with the penetration of injected fluid has been conducted by Haimson and Fairhurst (1967, 1969) and Haimson (1968). Detournay and Carbonell (1997) pointed out that the classical H-W model and the H-F model represent a condition of fracture initiation in the limiting case of fast and slow pressurization rates, respectively. Detournay and Cheng (1992) introduced a length-scale parameter around the wellbore in their breakdown model (D-C model) in which fluid diffusion along the length was considered. Degue and Ladanyi (2000) also mentioned that the effect of the pressurization rate on the BP is closely related to the extent of fluid penetration into the cracks. The radius of fluid penetration decreases with increasing pressurization rate.

Goodfellow et al. (2013) compared HF behavior in Westerly granite at two different injection rates of 0.2 ml/min and 0.5 ml/min under the same axial stress of 120 MPa and a confining stress of 5 MPa. In the case of the higher injection rate, BP, the maximum AE amplitude, the volume strain increment, *P*- and *S*- wave velocity changes, and the pressurization rate were greater than in the case of the lower injection rate. Zhuang et al. (2019a) measured water infiltration into granite core samples with diameters of 50 mm at seven different injection rates varying from 1 to 100 mm3/s. The pressurization rate, which was back-calculated from the injection pressure changes with injection time, increased with increasing injection rate, though the growth was nonlinear. A threshold injection rate exists for inducing breakdown under certain stress conditions. Below the threshold, injection fluid infiltrated into the sample gradually, and the sample became saturated without fracturing. A recent study reported that fluid permeation into mortar specimens during a time-delayed pressurization at a constant borehole pressure causes a decrease of 22% in BP as well as a mitigation of AE activities (Ha and Yun, 2020). In addition, Baptista-Pereira et al. (2020) found that fluid diffused into granite matrix and progressively pressurized the pre-existing flaws until cracks developed. We have noted that water saturation, fluid viscosity, and the injection or pressurization rate affect hydraulic fracturing results. This influence is attributed to fluid infiltration, and the topic is highlighted in the discussion section.

5.3. Stress state

The HF behavior of a rock sample is undoubtedly significantly influenced by the stress state applied to the sample. In general, in-situ stress usually has different magnitudes in the three principal directions. To reflect the three-directional stress state, a true triaxial testing system is required. In addition, for some rock types, intermediate principal stress plays a key role during rock breakdown, and the Mohr-Coulomb failure criterion is not valid (Labuz and Zang, 2012). Stress conditions, particularly differential stresses, could influence the HF mechanism. Fractures could switch from tensile failure to shear failure when the stress deviator increases to a certain magnitude (Lockner and Byerlee, 1977; Solberg et al., 1980). For a given borehole, induced hydraulic fractures are usually parallel to the maximum principal stress oriented perpendicular to the borehole. Both far-field stress and internal pressure in the borehole are responsible for the stress around the borehole and understanding the principal stress trajectories and stress magnitudes is of great significance for wellbore design and hydraulic fracturing operations (Thomas and Weijermars, 2018). Guo et al. (1993c) noted that in-situ stress dominates not only the orientation of the fracture initiation and propagation, but also the fracture length and width. The rate of fracture propagation decreases with an increase in the least principal stress. A laboratory experimental study by Zhao et al. (1996) revealed that far-field horizontal stresses largely influence the difference between the initiation pressure of HF and the BP. In case of horizontal differential far-field stress conditions, the initiation pressure of fracturing is typically 10–20% lower than the BP.

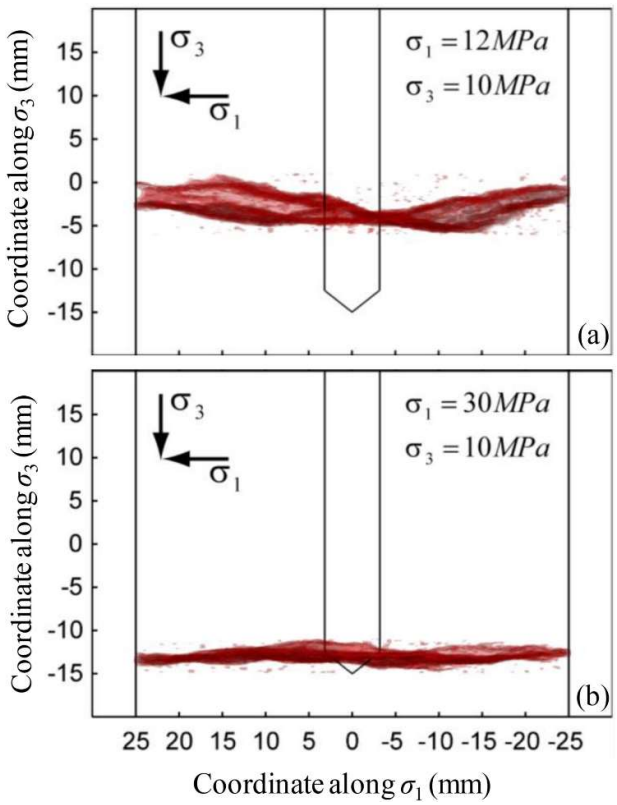

Figure 9. *Numerical modeling results of different fracture surfaces projected on the σ1–σ3 plane for (a) small (1.2) and (b) large (3.0) principal stress ratios (modified from Goodfellow et al., 2016). The fractures obtained from micro-CT reconstructions are indicated in red and have a voxel size of about 28 μm.*

Goodfellow et al. (2016) performed HF tests under four different stress states with a constant σ_3 of 10 MPa and σ_1 = 12, 15, 20, and 30 MPa, where σ_3 was applied parallel to the borehole and σ_1 was applied perpendicular to the borehole. Test results reveal that the microcracks tend to concentrate along one main fracture as both the stress ratio (σ_1/ σ_3) and the differential stress (σ_1–σ_3) increase, as shown in Fig. 9 and further confirmed by numerical simulations. Zhou et al. (2020) pointed out that the branch fractures were influenced by the magnitude of differential stresses and that the high differential stress restrains the expansion of fractures. This finding is consistent with experimental and numerical simulation results reported by Goodfellow et al. (2016).

6. Innovative injection schemes

The studies reviewed above focused mostly on conventional HF, which employs continuous injection until rock failure has been achieved. In recent years, induced or triggered seismicity by hydraulic stimulation treatments in EGS sites has raised the issue of environmental impacts, such as induced seismicity (Majer et al., 2007; Zang et al., 2014; Lee et al., 2019). New stimulation strategies, including fatigue hydraulic fracturing (FHF, Zang et al., 2013), multi-stage hydraulic fracturing (Meier et al., 2015), and cyclic soft stimulation (CSS, Hofmann et al., 2018), which applies various fluid-injection protocols, have been proposed as new tools to control hydraulic fracture growth and to prevent greater magnitudes of induced seismicity. The basic concept of hydraulic fatigue and its impact on fluid-injection-induced seismicity and the permeability-enhancement process is presented in Zang et al. (2019). For example, the main difference between cyclic hydraulic fracturing (CHF) and conventional HF is the frequent lowering of injection pressure (or injection rate) by cyclic injection to allow stress relaxation at the fracture tips. Induced seismicity by cyclic hydraulic fracturing is expected to be relieved due to the controlled release of crack-tip stresses. Fig. 10 compares different injection schemes for conventional HF and fatigue HF (FHF). Fig. 10a–c are injection-rate-controlled, while Fig. 10d–f are pressurization-rate-controlled injection schemes. In the next sections, we compare the experimental results of HF when applying the different fluid-injection schemes.

6.1. Cyclic hydraulic fracturing

Methods for mitigating induced seismicity by CHF were investigated through a series of laboratory hydraulic fracturing tests on granite cylinders with a diameter of 50 mm and a height of 100 mm (Zang et al., 2019; Zhuang et al., 2019b, 2020b) and on cubic blocks with side lengths of 50 mm and 100 mm, respectively (Zhuang et al., 2018b, 2020c). Some tests were combined with AE monitoring and CT analysis (Diaz et al., 2018a, 2018b, 2018c). Moreover, numerical modeling based on a discrete element method was conducted to enable a better understanding as to why CHF could help reduce the maximum magnitude of induced seismicity via fluid injection (Yoon et al., 2014, 2015a) at the beginning of the stimulation treatment.

Zhuang et al. (2019b) found that in the pressurization-rate-controlled test, induced fractures in the cylindrical granite sample showed more branching by cyclic injection compared with continuous injection. The authors also compared induced seismicity and permeability enhancement between continuous and cyclic injection under the injection-rate-controlled condition. The results show that CHF generally reduces BP by ~20% compared with the monotonic BP of continuous injection. The maximum amplitude of AE hits is reduced by an average of 13.7 dB. Moreover, laboratory HF and CHF tests were first compared on cubic samples with a side length of 50 mm using the same granite under true triaxial stress states of 20 MPa (vertical), 20 MPa (maximum horizontal) and 10 MPa (minimum horizontal), respectively (Zhuang et al., 2018a). Results reveal that CHF generates more intergranular fractures despite the fact that intragranular fractures dominated in both HF and CHF. Cyclic injection tends to form fracturing paths of least resistance because the tensile strength of the interface of quartz and feldspar grains is lower than that of individual quartz or feldspar grains for some granite (Savanick and Johnson, 1974).

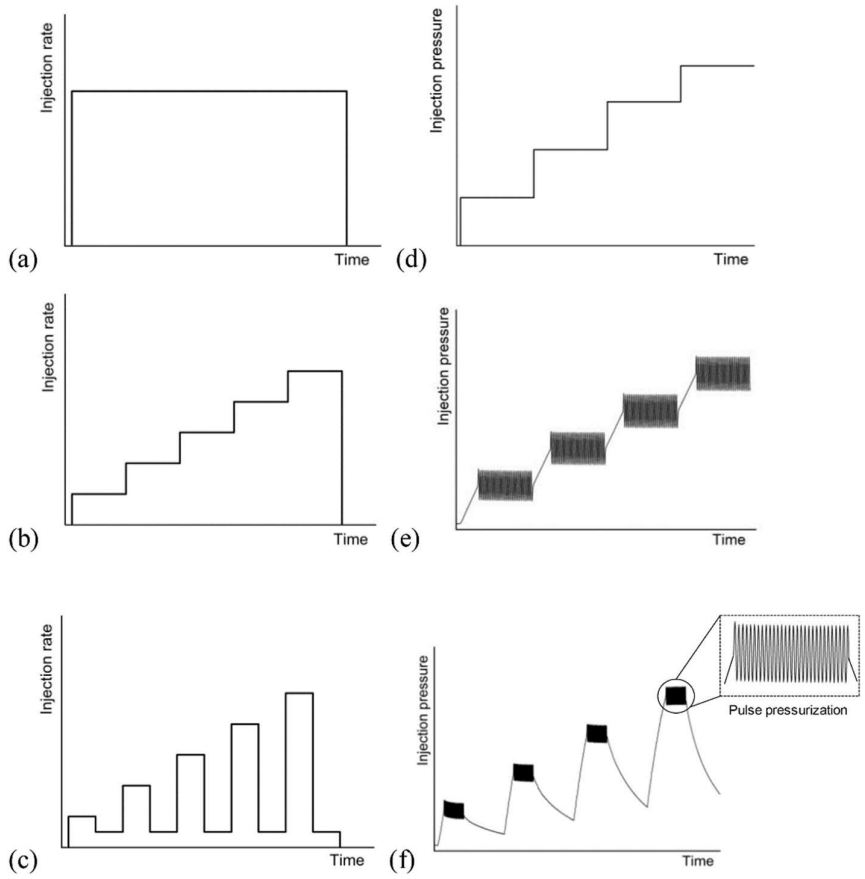

Figure 10. *Three injection-rate-controlled injection schemes (a–c), and three pressurization-rate-controlled fluid-injection schemes (d–f) used in laboratory hydraulic fracturing tests. (a) Constant-rate continuous injection, (b) Stepwise-rate continuous injection, (c) Cyclic progressive injection, (d) Stepwise pressurization (SP), (e) Stepwise pulse pressurization (SPP), and (f) Cyclic pulse pressurization (CPP) (modified from Zhuang et al., 2020c).*

Fig. 11 compares 3D structures of typical hydraulic fractures in HF and CHF after testing reconstructed by CT. The HF sample in Fig. 11a shows a planar fracture cutting across grains. In the CHF sample (Fig. 11b), the main fracture propagates along the grain boundary in the vicinity of the borehole, and intergranular and intragranular fractures alternate. Moreover, there are a number of fracture branches. The estimated total volume of the extracted fractures is 19 mm^3 for the HF sample, and 78 mm^3 for the CHF sample. Assuming that the fractures have a uniform aperture, the average aperture (the ratio of fracture volume and fracture surface area) is 0.106 mm for the HF sample and 0.073 mm for CHF sample. Fractures created by HF tend to have a larger aperture on average than those created by CHF. As the two samples have different sizes, we compared the ratio of the total surface area of fractures and the sectional area of the XZ plane. This parameter is similar to the parameter of the fractal dimension used for evaluating the complexity of fractures by Ishida et al. (2012). For the ideal case of a flat fracture along the cross-section, the ratio is 1.0. The calculated ratio of the two areas is 1.10 for the HF sample and 1.76 for the CHF sample. The larger magnitude of the ratio indicates that the fractures have a rougher profile. Fractures in CHF have a more undulated fracture plane compared with the fractures in conventional HF (which are more planar fractures).

The main purpose of HF is to enhance the permeability or injectivity of rock formation. Unlike permeability, the injectivity index refers to the rate at which fluid can be injected into a well at a given pressure differential. However, both parameters can be used to evaluate the hydraulic performance of a rock mass. It has been reported that injectivity enhancement on the Pocheon granite by CHF was less pronounced compared with conventional HF, in both triaxial HF tests (Zhuang et al., 2019a) and true triaxial HF tests when considering a horizontal differential stress of 10 MPa (Zhuang et al., 2018a). However, previous studies have reported that CHF achieves better permeability enhancement than conventional HF in laboratory experiments on cylindrical Tennessee sandstone samples with 6% porosity (Patel et al., 2017). The observed process zone generated by cyclic injection is twice that induced by conventional fracturing. CHF increases fracture permeability compared with conventional HF by a factor of between 3 and 10. These findings indicate that CHF has advantages for sandstone in terms of both BP reduction and permeability enhancement. The differences in findings related to the permeability enhancement by HF and CHF are closely related to the rock type and stress

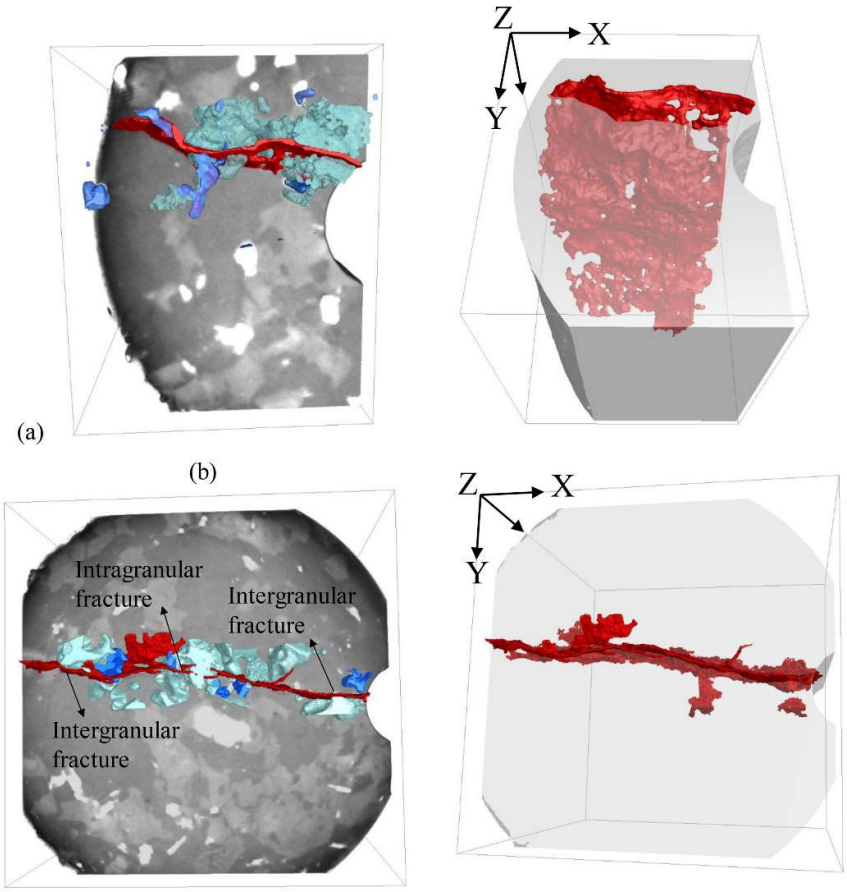

Figure 11. *CT images of hydraulic fractures created by (a) continuous injection (block size 11.5 mm × 14.2 mm × 14.3 mm) and (b) cyclic injection (block size 24.9 mm × 24.7 mm × 24.3 mm). The left panels show the locations of the fractures and mineral grains (top view), and the right panels show fracture planes in space (side view). Fractures are in red, and minerals are in other colors (mint = feldspar, blue = mica, grey and white = unidentified minerals).*

state as well as the injection pattern. These findings require further investigation.

6.2. Fatigue hydraulic fracturing

Fatigue hydraulic fracturing is a general term used to group hydraulic fatigue processes in rock mass using pressure cycles and pressure oscillation/pulses (Zang et al., 2013, 2019). The first FHF mine test application in the Äspö Hard Rock Laboratory (HRL) demonstrated a combination of cyclic and pulse hydraulic fracturing (Zang et al., 2017). Fluid is injected in pressure cycles with increasing target pressure separated by depressurization phases to relax the crack-tip stresses. During pressurization phases, the target pressure level is modified via pulse pressurization generated by a second pump system. Experimental results in the Äspö HRL indicate that the combination of two pumps with multiple-flow rates allows a more complex fracture pattern to be designed with arresting and branching fractures that form a broader fracture process zone (Zang et al., 2017).

The FHF technique was demonstrated at the Äspö HRL in formations of granite and granodiorite (Zang et al., 2017, 2019). Three different water-injection schemes, including continuous injection, cyclic progressive injection and a combination of cyclic injection and pulse pressurization, were compared in a mine-scale in-situ test. Experimental results reveal that by progressively increasing the target pressure interrupted with intervals of low pressure, the total number and magnitude of acoustic events can be reduced. Further, a full-waveform detection and localization method using data from the in-situ experiments indicates that seismic *b*-values are larger in the combination of cyclic injection and pulse pressurization as compared with conventional HF treatment (Niemz et al., 2020). The increase in permeability of the combined progressive cyclic and pulse treatment was five times the permeability enhancement of the conventional fracturing in the same rock type of granodiorite at Äspö HRL (Zimmermann et al., 2019). The combination of cyclic progressive injection and pulse pressurization showed the best hydraulic performance of all the three tested schemes. The mechanism of permeability evolution and induced-seismicity reduction, however, can be different for different rock types.

The injection scheme described above, which combines cyclic progressive injection and pulse pressurization, was also tested in the laboratory under pressurization-rate control using one hydraulic pump only, and this scheme was defined as cyclic pulse pressurization (CPP). Zhuang et al. (2020c) conducted true triaxial HF tests

together with AE monitoring on 100-mm cubic granite samples and compared the three injection-rate-controlled injection schemes (Fig. 10a–c) and the three pressurization-rate-controlled injection schemes (Fig. 10d–f). For the stepwise pulse pressurization (SPP, Fig. 10e) and CPP (Fig. 10f) injection scenarios, pulse pressurization was applied at the target pressure level in each step, while the loading frequency and the amplitude were varied. AE monitoring was applied to investigate the fracture initiation and propagation process. The associated induced seismicity was evaluated based on amplitudes of AE hits, the AE hit rate, and seismic energy (Diaz et al., 2018c). The fold of increase (FOI) of injectivity and the maximum amplitude of AE that had occurred during the fracturing for the six injection schemes are compared in Fig. 12. The CP scheme has the lowest induced seismicity, while the improvement in injectivity is the least pronounced. The SPP scheme has the highest injectivity among all schemes. The CPP scheme allows for increasing injectivity and decreasing induced seismicity and is a promising alternative injection scheme. As AE energy is generally proportional to the squared AE amplitude, the data of the two groups are fitted by parabolic curves, which show $y = 0.006(x - 60)^2$ for injection-rate-controlled tests and $y = 0.036(x - 67)^2$ for pressurization-rate-controlled tests. This interesting finding indicates that the injectivity FOI depends more strongly on the AE energy for the pressurization-rate-controlled tests. Permeability increase is less pronounced using flow-rate-controlled test; at the same time, however, larger seismic events are expected compared with pressure-controlled tests.

By comparing the average fracture length for different injection schemes, Zhuang et al. (2020c) found that fracture propagation is more persistent and longer, particularly if the injection pressure is increased continually without depressurization. A possible link between rock fragments – in particular, quartz chips (which act as natural proppants) – and pulse pressurization was observed. These rock fragments did not plug the fracture but instead acted as stress concentrators at the fracture tip for further persistent fracture growth, which resulted in relatively larger fracture lengths (Zhuang et al., 2020c). The laboratory tests demonstrate the potential for hydraulic fracture-growth control via advanced fluid-injection schemes, which can also prove beneficial when applied in the field, thereby allowing for more controlled fracture network engineering via hydraulic stimulation treatments.

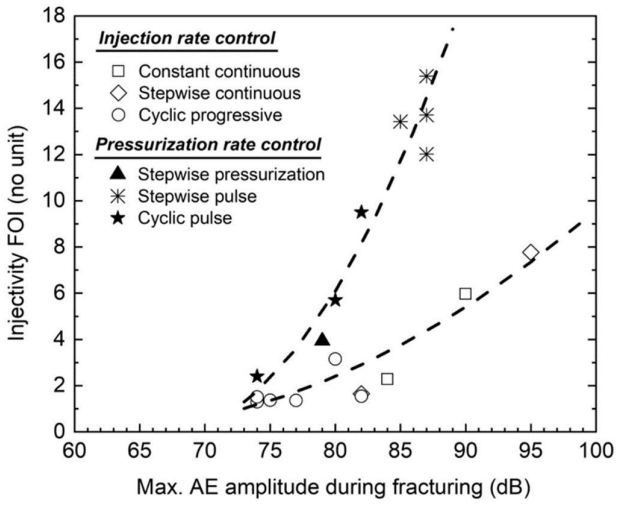

Figure 12. *Comparison of injectivity FOI (Y-axis value), plotting versus the maximum amplitude of AE hits (X-axis value) for the six injection schemes defined in Fig. 10. FOI: fold of increase. The data of the injection-rate- and pressurization-rate-controlled injection schemes were fitted by parabolic curves. (modified from Zhuang et al., 2020c).*

7. Fracture inspection

Fracture patterns are highly critical in EGS reservoir stimulation, which aims to maximize the productivity of geothermal resources. In the laboratory, the observation of induced fractures can be classified into two types: non-destructive and destructive. Non-destructive testing methods used for investigating fractures are mainly limited to AE monitoring or ultrasonic testing, X-ray CT scanning, and the photometric method. Similar to optical imaging using a downhole camera, some studies have applied endoscopes to obtain images of the borehole during laboratory experimental HF tests (Ha et al., 2017). The X-ray CT method is widely used in various areas because it is very convenient for obtaining 3D structures of scanned objects to evaluate changes to a sample internal structure. The photometric method has been widely used to measure deformations of soil and rock; however, it has rarely been seen in HF tests. This method is only able to measure visible deformations, and the object of observation must therefore be transparent in order to allow the observation of internal changes, such as the impermeable material PMMA (**P**oly**m**ethyl **m**eth**a**crylate) (Rubin, 1983; Kovalyshen et al., 2014; Frash et al., 2016). However, artificial materials such as PMMA are limited to theoretical study as they are much different from rock materials in their physical and mechanical properties and therefore also in their engineering behavior.

The destructive method is to cut the specimen after the test for direct observation via microscopic-image analysis. This method is usually combined with the injection of a dye-laden fluid, such as dyed water, to improve the visibility of fractures (Zhou et al., 2010; Fan and Zhang, 2014), or with the post-processing of samples using blue epoxy (Stanchits et al., 2011), an acrylic resin mixed with a fluorescent substance (Chen et al., 2015). The testing sample is cut to make a thin section, which is observed via microscope (Brenne et al., 2013; Stoeckhert et al., 2015; Chen et al., 2015; Patel et al., 2017; Zhuang et al., 2020c). This method is able to detect fractures at the mineral scale. However, it is exceedingly difficult to obtain reliable 3D structures of fractures. A 3D laser-scanning technique was used to obtain the morphology of the fracture surface and to measure its roughness (Wang et al.,

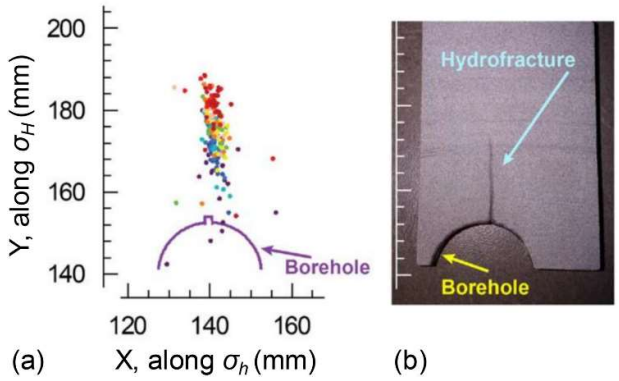

Figure 13. *AE analysis of hydraulic fracture propagation in sandstone. (a) AE hypocenter distribution within the sample slice and (b) hydraulic fracture growth path from the borehole wall in the direction of maximum stress. The color of the dots corresponds to the time sequence of the AE events: Violet indicates the earliest AE events, red the latest AE events. X and Y are the coordinates that correspond to the maximum and minimum horizontal stresses (σH, σh), respectively (modified from Stanchits et al., 2012).*

2019a). The destructive method has several limitations. For example, the sample or the hydraulic fractures could be disturbed by cutting, or it could be impossible to observe the fracturing process if the sample has been destroyed.

7.1. Acoustic emission monitoring

Understanding the initiation and evolution of fractures is very important for deriving a model to predict fracturing processes. Thus far, AE monitoring is the most effective method for monitoring the initiation and propagation of brittle fractures, and the parameters obtained from waveforms help in analyzing the fracturing mechanism. AE monitoring has therefore often been applied in experimental studies of fracturing process of concrete as well as rock (Hartman, 1977; Lockner, 1993; Zang et al., 1996, Zang et al., 2000; Ohtsu et al., 1998; Stanchits et al., 2006). Lockner (1993) provided a systematic review of the applications of the method in the study of rock fractures. The ISRM suggested method for laboratory AE monitoring, that includes an experimental setup and data-analysis protocols has also been reported (Ishida et al., 2017).

For most laboratory HF tests, the dimensions of rock fractures are considered to be range from microns to centimeters and to be related to the grain size of the type of rock under investigation. Laboratory AEs correspond to a range of frequencies, from MHz to kHz (Lei and Ma, 2014). The first important step in AE monitoring is to select and install sensors. Different sensors have different sizes and ranges of frequency measurements. Diaz et al. (2018a, 2018b, 2018c) use Nano30 sensors (8 mm in both outside diameter and height) with an operating frequency range of 125–750 kHz. At least five sensors or four sensors and one other piece of information are required to obtain a 3D location of AE events (Ishida et al., 2017). Each AE event corresponds to a source or location of crack initiation. Locations of AE events therefore indicate the locations of induced fractures inside samples. Six to sixteen sensors have frequently been used in previous studies (see Table 1 and 2). For a good AE source location, a three-dimensional array of sensors with different relative locations between one another is preferred, and the sensors must be adhered to the sample directly using a couplant, such as grease or wax. The accuracy of the measured locations of the AE events is influenced by many factors (Hampton et al., 2019), particularly the total number of sensors and the selection of the wave velocities of the material. The accuracy of the source location can range from 5 mm for a 279 × 279 × 381-mm sandstone block (Stanchits et al., 2012) to 2.5 mm for granite samples (50 mm diameter, 100 mm height) during triaxial compression tests (Stanchits et al., 2006). Ishida (2001) reported a location error of 10 mm for a 200 × 200 × 200-mm granite block during hydraulic fracturing tests. Ji and Wu (2020) carried out triaxial shear-flow experiments on Bukit Timah granite cores with saw-cut and natural single fractures inside. They used three AE sensors to monitor the strain energy release rate from the fracture and compared relative AE signals obtained from different experiments. Pre-amplitude gain and amplitude threshold were set to 40 dB, and the sampling frequency was 1 MHz. This setup is comparable to brittle triaxial fracture experiments on dry granite (Lockner, 1993) except for the number of sensors used. At the laboratory scale, applying four or more AE sensors allows for hypocenter tracking of microfracturing events and for a detailed determination of the source mechanism during both the brittle and hydraulic rock-failure process.

If loading plates directly contact sample surfaces and three directional stresses were applied, AE sensors are usually attached to the loading plates (Frash, 2014; Diaz et al., 2018a) or close to the corners of the cubic samples (Diaz et al., 2018c). In one study, grooves and holes were made in loading plates or surfaces of granite samples for placing AE sensors and cables (Ishida et al., 2016; Xing et al., 2019). The AE system must be calibrated before the main experiment. Background noise should be minimized by selecting a suitable threshold for the AE amplitude. The pencil-lead break test is one simple method for verifying that sensors work well and for testing the background noise. The ball-drop test is more widely applied for calibrating the source and absolute energy of AE signals (Zang et al., 2000; McLaskey et al., 2015).

As has been shown in previous standard references (Ishida et al., 2017), several parameters for further AE analysis can be obtained for a recorded waveform: AE duration, rise time, AE amplitude, and AE count. One AE hypocenter indicates the location of the AE source where a cracking or sliding event has occurred. One event can be detected by several sensors at the same or different times, and multiple AE hits thus correlate to one source location. Different parameters obtained from monitoring results

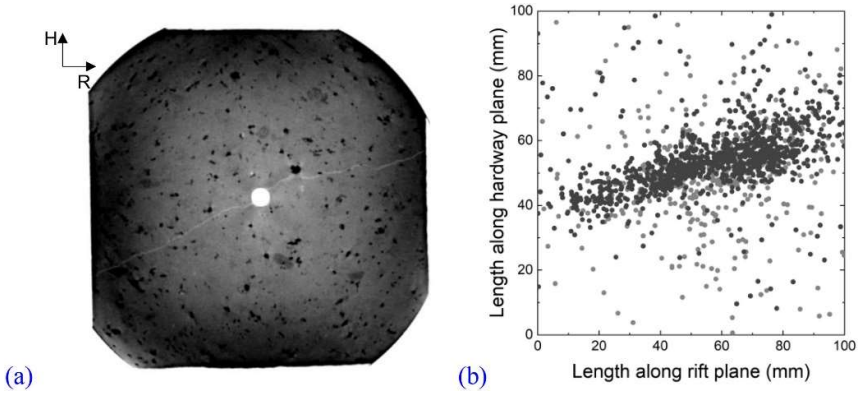

Figure 14. *AE event location on hydraulic fractures in Pocheon granite subjected to cyclic progressive injection. (a) A 2D CT image shows the hydraulic fractures generated on both sides of the borehole, and the fractures slightly deviated from the direction of rift plane; H-hardway, R-rift; (b) Planar location of AE events, with light grey dots corresponding to a period of 5 s (immediately before and after the main breakdown), and dark grey dots corresponding to the next period of 100 s (re-injection into the fractured specimen).*

such as the AE hit, AE count, AE rate, AE event rate, cumulative AE (events), AE energy (rate), and amplitude have been used in a number of references. It is necessary to differentiate between the meanings of parameters with similar names. Evolutions of AE count rate, accumulative AE hits/counts, or the seismic *b*-value of the Gutenberg–Richter distribution with injection time are frequently used for analyzing the initiation and propagation of hydraulic fractures (Stanchits et al., 2012; Ishida et al., 2012; Damani et al., 2013; Chitrala et al., 2013; Goodfellow et al., 2016). A higher *b*-value stands for more small-magnitude induced seismic events, which renders the treatment safer.

Fig. 13 shows a typical example of AE monitoring results of hydraulic fracture initiation and propagation from a borehole in sandstone (Stanchits et al., 2012). AE hypocenters mapped during testing (Fig. 13a) match with the hydraulic fracture observed from the cross-section of the fractured sample after a test (Fig. 13b). The sandstone block used in the study had dimensions of 279 × 279 × 381 mm, and a combination of AE and ultrasonic transmission (UT) monitoring was applied in the HF tests. Measurements of *P*-wave velocity and *P*-wave amplitude could be obtained from UT monitoring. Using the monitoring system and an additional data-processing-software package, the accuracy of the AE hypocenter localization was reported to be about 6 mm.

Fig. 14 shows an example of an AE event location in a Pocheon granite block, which was fractured by cyclic progressive injection during a hydraulic fracturing test. The specimen had a side length of 100 mm, and true triaxial stresses were applied to the six surfaces. Eight Nano-30 sensors were installed at the eight corners of the specimen (Zhuang et al., 2020c). According to CT scan results, bi-wing fractures were generated and deviated slightly from the direction of rift plane (Fig. 14a). The locations of the AE events (Fig. 14b) essentially aligned with the hydraulic fracture.

Moreover, AE monitoring results can be used to analyze failure modes (tensile, shear, or mixed-mode) based on a moment tensor analysis (Ohtsu et al., 1998; Chang and Lee, 2004; Hampton et al., 2014, 2018), first pulse polarity statistics (Zang et al., 1998), or a method that combines two AE parameters of rise angle (RA) and average frequency (AF), as suggested by the RILEM Technical Committee (2010). The RA is calculated as rise time divided by the maximum AE amplitude, while AF is the ratio of AE counts and AE duration. Fig. 15 shows an example of the analysis result based on the RA-AF method that applies the criterion of AF=100*RA. Under the specific test conditions, AE hits with relatively large magnitudes of amplitudes are likely to have been tensile-crack-correlated. The analysis result can be referenced when investigating the fracturing-source mechanism. However, there are no clear criteria for selecting the ratio of AF and RA to decide the boundary of tensile and other types of cracks. A ratio of 1/10 for RA/AF was applied to separate shear and tension cracks in granite samples induced by HF (Diaz et al., 2018a, 2018b). Focal mechanism analysis via picking up the P-wave first motion polarities in a single waveform is more frequently used to identify tensile or shear cracks (Zang et al., 1998; Lei et al., 2000; Ishida et al., 2000). This method is more reliable than the RA-AF method for crack-mode determination; however, it is more time-consuming to manually choose the first motion of each waveform for all the events. Automated choosing and full-waveform methods are currently in development.

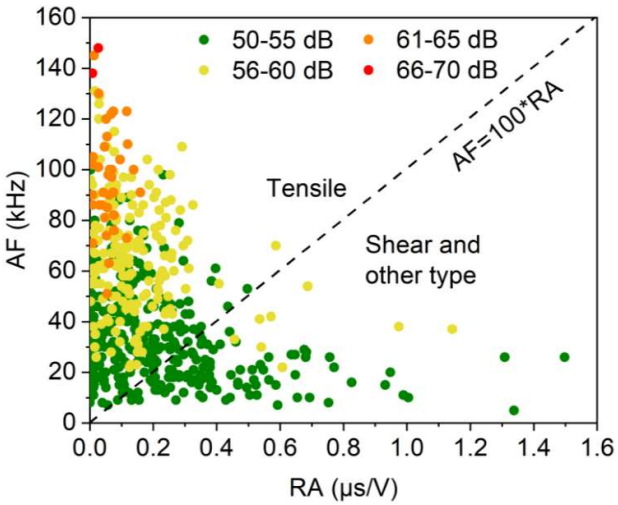

Figure 15. *Crack-mode classification based on RA-AF parameters obtained from AE monitoring results during true triaxial HF tests on a cubic granite sample. The AE hits were divided into four groups (delineated in different colors) based on their magnitudes of AE amplitude in dB.*

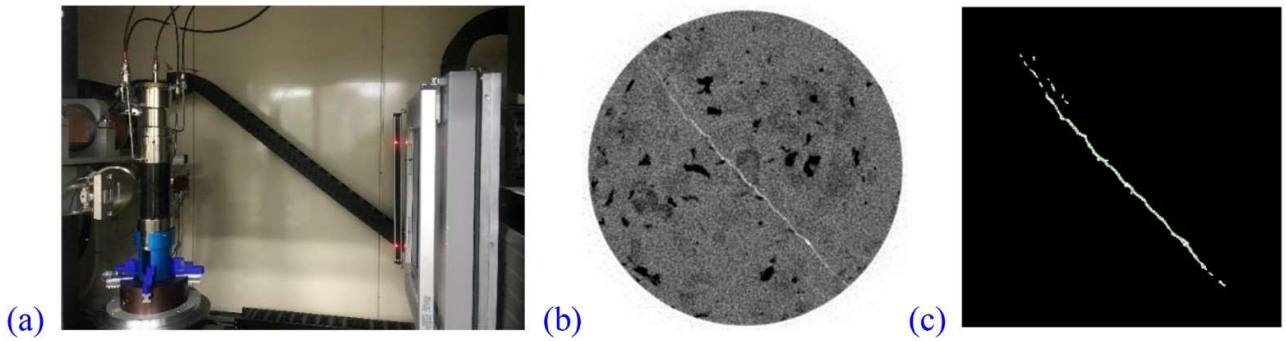

Figure 16. *Hydro-mechanical laboratory testing of rock combined with in-situ X-ray CT scanning: (a) Test equipment in an X-ray chamber, (b) a 2D CT image of granite cylinder (38 mm in diameter) containing a single fracture at 5 MPa of confining pressure, (c) a fracture segmentation based on Hessian matrix filtering and Otsu's method (modified from Zhuang et al., 2020d).*

AE amplitude or AE energy was used to evaluate induced seismicity during hydraulic fracturing experiments (Zhuang et al., 2019b; Diaz et al., 2018a, 2018b, 2018c; Zang et al., 2017, Zang et al., 2019; López- Comino et al., 2017). AE amplitude can be used as a reference value for evaluating seismic energy since the energy is generally proportional to the amplitude square. To evaluate seismic energy quantitatively and more precisely, a sophisticated calibration of AE sensors is usually required. Ball-drop experimental results have shown that the amplitude from a broad-band AE sensor of 1 mVs is calibrated to account for an absolute energy value of 33 μJoule in the case of a granite from Erzgebirge Germany (Zang et al., 2000). More information on sensor calibration for using absolute energy in AE studies on rock can be found in the review article by Ishida et al. (2017).

We view radiated seismic energy as an important parameter obtained from AE monitoring in rock-failure studies because the radiated seismic energy and fracture-surface energy obtained from microscopic or X-ray CT inspections are primary data required to obtain information on the overall energy budget involved in hydraulic fracture growth. Apart from the total deformation energy stored in the specimen, in fluid-injection experiments, the hydraulic energy pumped into the system is of additional interest (Goodfellow et al., 2015). To determine the radiated seismic energy, AE sensors with a calibrated transfer function are preferable, as has been documented in deformation experiments on granite (Zang et al., 1998) and on dry and wet sandstone (Zang et al., 1996). Determining magnitude–frequency distributions is the next step in data analysis (Lei et al., 2016; Goodfellow et al., 2015). A change in AE events rates can be used to discriminate failure regimes, particularly the tipping points of cumulative failure mechanisms (tensile versus shear dominated).

Apart from cumulative event counting and event-rate analysis, multi-sensor arrays allow for hypocenter tracking and an in-depth analysis of the source mechanism (Manthei, 2005; Schubnel et al., 2007; Ishida et al., 2012). A trend in source location is first to use re-located events (e. g., the double-difference method; Waldhauser and Ellsworth, 2000) and second to replace the standard first-pulse hypocenter-location technique with the full-waveform location method (Niemz et al., 2020). Crack-type analysis today is based on moment-tensor inversions (Kwiatek et al., 2014; Manthei, 2017; Yamamoto et al., 2019). More tensile cracks are commonly observed in the initial loading and failure preparatory phase, while in the failure- and post-failure regime, more high-energy shear cracks are observed. This holds for brittle rock failure (Zang et al., 2002) and fluid-injection-induced rock breakdown (Diaz et al., 2018c). The analysis of amplitude spectra for individual seismic sources with different magnitudes allows for determining the corner frequency of events, which yields additional information on the crack-source process (McLaskey et al., 2014; Petružálek et al., 2020).

7.2. X-ray computed tomography measurements

AE monitoring has limitations for determining the accurate location of fractures in small samples and for evaluating the geometric properties of fractures, whereas another nondestructive method of 3D image reconstruction – namely that using X-ray Computed Tomography (CT) – can overcome these limitations.

Industrial X-ray CT scanners are typically used for laboratory study on various materials, including construction materials. Details about the CT system and image processing can be gleaned from Ketcham and Carlson (2001) and from the standard guide for CT imaging (ASTM, 2011). Cnudde and Boone (2013) reviewed the advantages and limitations of micro-CT (μCT) and its applications in the geosciences. In some recent studies of HF tests, CT scanning has been used to quantitatively evaluate hydraulic fracture properties, such as fracture aperture (Watanabe et al., 2017a; Kumari et al., 2018; Zhuang et al., 2019a), fracture volume (Hampton et al., 2014, 2018; Zhuang et al., 2020a), fracture length (Goodfellow et al., 2013), and tortuosity (Diaz et al., 2016a; Liu et al., 2018). These geometric parameters of fractures can be used to evaluate permeability enhancement by fracturing. In addition, CT observations at the grain scale can provide a better understanding of hydraulic fracturing mechanisms, such as the separation of grain boundary fractures

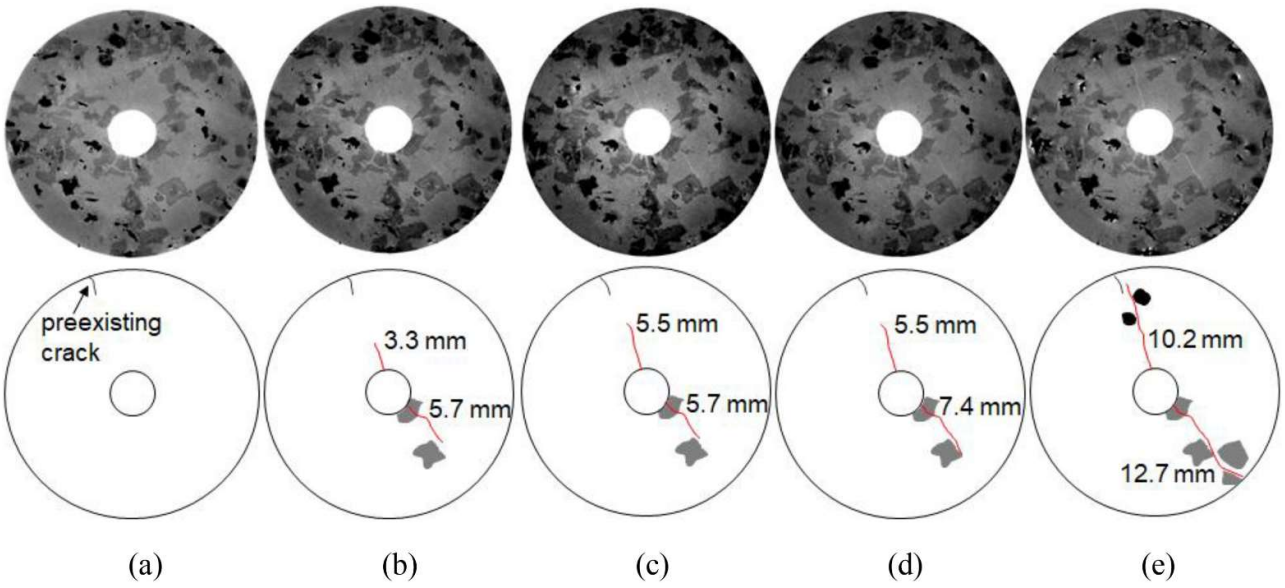

Figure 17. *Ex-situ X-ray CT images (upper panel) and corresponding sketches (lower panel) showing fracture evolution under cyclic injection: (a) Initial state, (b) after 20 cycles, (c) after 25 cycles, (d) after 28 cycles, and (e) after 29 cycles. For the sketches: red line = hydraulic fracture; grey = feldspar grain; black = mica grain. Values represent the total length (unit: mm) of fracture at each side of the borehole. (modified from Zhuang et al., 2020b).*

and intragranular fractures (Kumari et al., 2018; Zhuang et al., 2018a). CT has the advantage that it can reconstruct the 3D morphology of discontinuities in rock, which can be implemented during the fracturing process. A study using synchrotron X-ray μCT investigated fracture propagation in a limestone sample with only a 9- mm diameter in which fractures were propagated by connecting pores and avoiding hard grains (Renard et al., 2009). Ju et al. (2018) applied in-situ CT to investigate the evolution of fractures in coal samples during mechanical loading during which loading was stopped from time to time to allow for a CT scan, at which point compressive pressure was maintained through servo control. A recently developed in-situ piece of CT equipment named "GEOACT" was reported by Li et al. (2020b). This equipment can provide a maximum axial force of 2,000 kN, a maximum confining pressure of 50 MPa, a seepage pressure and a gas pressure, and a temperature range of -40–200°C and is capable of in-situ CT imaging of mechanical and hydro-mechanical tests on samples with a diameter of 50–100 mm. Using the equipment described above, a shale sample was fractured at 42.42 MPa via supercritical CO2 injection under 30 MPa of confining pressure, and fractures with measured apertures of about 0.5 mm were captured via in-situ CT imaging. However, the image resolution was not reported. More recently, Zhuang et al. (2020d) reported hydro-mechanical testing on rock under confining pressures of 0~20 MPa, and 3D CT images were obtained at about 400 seconds (<10 minutes, including overhead time) at a resolution of 67 μm/pixel for a granite sample with a diameter of 38 mm (Fig. 16). The equipment enabled a quantitative evaluation of fracture-aperture changes with confining pressure as well as with fracture-surface roughness.

The resolution of CT images is significantly influenced by the sample size as well as by the density of specific minerals and crack elements. Very thin cracks in granite samples can be enhanced by a potassium iodide solution (Ohtani et al., 2000) or by other chemical solutions with similar functions. It is important to try to reduce the sample size for obtaining high-quality CT images on the premise that the sample size is suitable for obtaining reasonable testing results. Moreover, depending on the sample size and scan conditions, it can take up to one hour or more to complete a typical industrial CT scan. It is therefore difficult to catch the catastrophic failure of a sample or to investigate real-time changes inside the sample. To observe water-induced hydraulic fractures at the grain scale, testing samples are required to have relatively small sizes that yield an acceptable resolution.

Cyclic hydraulic fracturing tests on cylindrical granite samples with a diameter of 30 mm and a borehole diameter of 5 mm were performed in the laboratory combined with CT scans (Zhuang et al., 2020b). The injection was stopped several times with an increasing number of cycles, and the sample was removed from the equipment for CT scanning free of external stresses: the so-called ex-situ CT scanning. Even though the CT scan was not in situ, the process of fracture initiation and propagation during a total of 29 cycles of water injection was captured, as shown in Fig. 17. A fracture was generated near the borehole during Cycle 20 (Fig. 17b), a bi-wing fracture was generated at Cycle 25 (Fig. 17c), and the two wing fractures extended gradually to the sample boundary with an increasing number of cycles. At Cycle 29, a fracture that extended along feldspar and mica grains was confirmed (Fig. 17e).

CT scanning has size limitations. The spatial resolution in a CT image is mainly influenced by the size of the focal

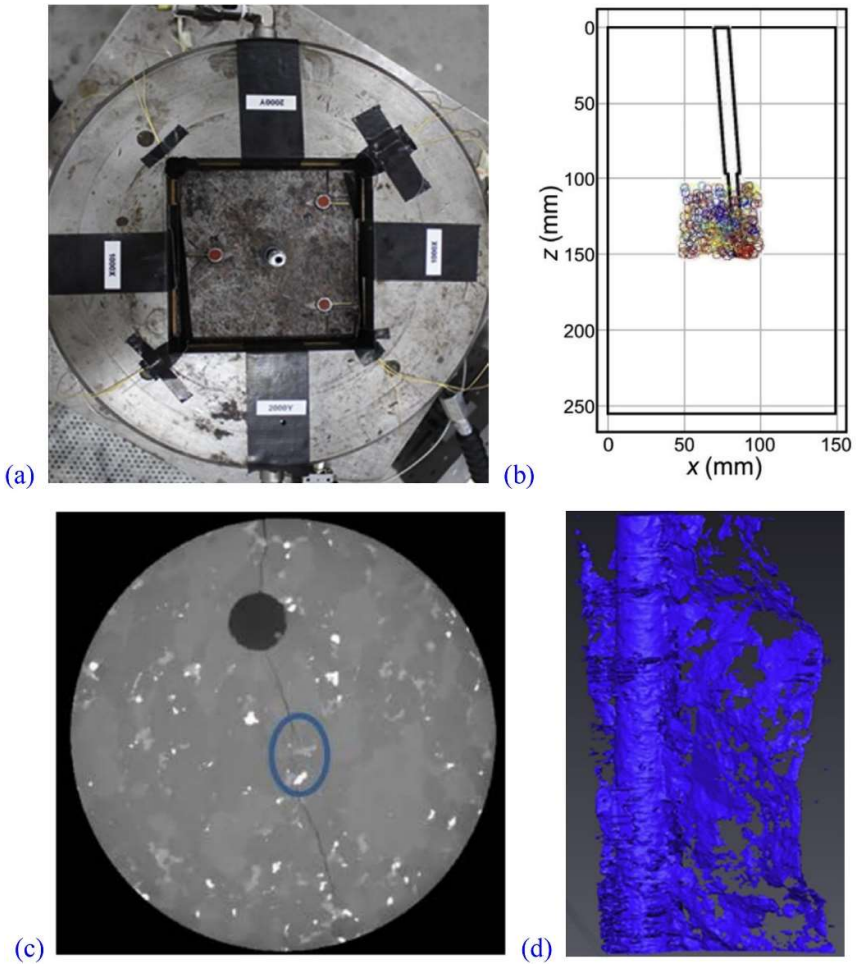

Figure 18. *A typical case of AE monitoring and CT imaging used for hydraulic fracturing experimental study in granite. (a) Installation of AE sensors in a cubic granite specimen, and (b) front view of AE event location based on moment tensor analysis. The open circles in different colors correspond to tensile, shear and mixed mode cracks. (c) 2D CT image of the cored sample (50 mm diameter, 150 mm height) including the wellbore. The ellipse marker shows the fractures interrupted by high density minerals (in white dots), and (d) 3D reconstruction of fractures (in blue) with open spaces correspond to discontinuities of the fractures. (modified from Hampton et al., 2014, 2018).*

spot, the size and number of the detector elements, as well as the magnification (the ratio of the source-to-detector distance to the source-to-object distance). To obtain high-resolution CT images, particularly for hydraulic fracture analysis, core samples that contain the region of interests (e.g., near the borehole) are cored from the original large sample used for the hydraulic fracturing tests (Hampton et al., 2014, 2018; Zhuang et al., 2018a, 2020c). In addition, low-resolution CT images could be further enhanced by post-processing techniques combined with a deep-learning method, which also enable automatic detection of fractures and pores from CT images of rock samples (Wang et al., 2019b). Fig. 18 shows a typical example of experimental study on HF of granite applying combined AE monitoring and CT imaging (Hampton et al., 2014, 2018). Referring to the AE event location results (Fig. 18b), granite cylinder (50 mm diameter and 100 mm height) for scanning was cored from the cubic granite sample (150 × 150 × 250 mm^3) with the borehole center deviated from the cylinder center (Fig. 18c). CT images were obtained at a resolution of 40 μm and allowed for fracture detection and segmentation. The influence of high-density mineral and fracture volume are further analyzed in the study.

7.3. Microscopic investigations

The method of combining a thin section and microscopy, for example, with a polarizing microscope, has been very frequently used to observe minerals and discontinuities and to measure fractures at the mineral scale (Chen et al., 2015; Ishida et al., 2016; Patel et al., 2017; Watanabe et al., 2019; Zhuang et al., 2020c). Ultraviolet light irradiation combined with fluorescent resin has been reported to the improve the observation of hydraulic fractures and very thin microcracks in granite samples (Chen et al., 2015; Ishida et al., 2016; Ye and Ghassemi, 2018; Watanabe et al., 2019). Acrylic resin that contains a fluorescent compound is imbibed to the fractured sample after testing, and the thin section is observed under ultraviolet light. A typical example of fractures in a Kurokamijima granite sample fractured by supercritical CO2 that is observed using the fluorescent method is shown in Fig. 19 (Ishida et al., 2016). The method also shows good results for observing a network of microcracks in granite (Watanabe et al., 2019).

Figs. 20 and 21 compare microscopic investigations of hydraulic fracture patterns in a tight sandstone and granite at the micrometer- or sub-grain scale. The tight sandstone has larger porosity (6%, Damani et al., 2013) compared with that of the granite (0.66%, Zhuang et al.,

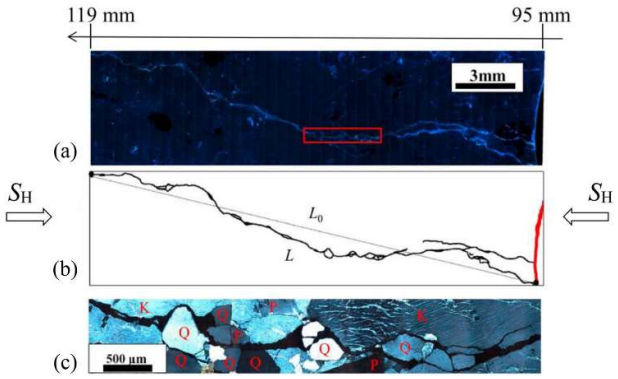

Figure 19. *Fracture growth path observed on thin sections using the fluorescent method. (a) Photo taken of the thin section, (b) sketches of the main crack. L is the total length of the fracture, tortuosity is computed from L/L0, and (c) details about the fractures and minerals shown via microscopic image taken under polarized light and that correspond to the red box part in (a). Q stands for quartz, P for plagioclase, and K for K-feldspar (modified from Ishida et al., 2016).*

2019a), while the two types of rock have a similar permeability of around 0.01 mD. The relatively high permeability for the granite can be attributed to the abundance of natural microcracks. Fractures are classified into intergranular and intragranular categories, with intragranular fractures being tensile induced, while intergranular fractures are either tensile or shear. HFs in sandstone are influenced by pores, and microcracking occurs in the vicinity of the main fracture. In granite, quartz (Qz), microcline (Mc), and orthoclase (Or), grains are the three dominant minerals. Intragranular fractures that cut the three different grains and intergranular fractures of Qz-Or, Mc-Or, and Mc-Qz were mainly observed. The grain size and mineral influenced the propagation of HF (Fig. 21). These results on fracture patterns help us to better understand the mechanism of hydraulic fracturing. Zhuang et al. (2020c) applied the microscopic method to the observation of HFs induced by different injection schemes. Facture lengths of intragranular fractures in different grain minerals and intergranular fractures as well as tortuosity were measured and compared. Results reveal that quartz grains are easily split compared with Or and Mc, and rock chips of quartz grains were frequently observed inside hydraulic fractures, particularly when quartz grains were adjacent to orthoclase or microcline grains. The natural proppants (e.g., quartz chips) play a key role in forming dendritic fractures (Kiel, 1977) and particularly in the fatigue hydraulic fracturing process (Zang et al., 2019) because quartz fragments that are removed from fracture walls by pulse pressurization and transported toward the fracture tip can change the local stress field. Local stress changes as compared with conventional hydraulic fracturing can cause a broader fracture damage zone to form, which allows permeability to be increased by a factor of 5–10 compared with conventional HF in both sandstone (Patel et al., 2017) and granitic rock (Zimmermann et al., 2019).

8. Discussion and implications for field applications

8.1. Infiltration zone and breakdown models

The apparent ambiguity between the H-W criterion and the H-F criterion (Fig. 1 and Eqs. (1) and (2), different fracture initiation pressures) can be resolved by introducing a flaw in the borehole wall from which the fracture growth initiates (Ito and Hayashi, 1991) because the fluid-pressure distribution in the borehole wall crack itself is a function of the injection rate. In the "fast pressurization" limit, the fluid pressure is assumed to be zero (Fig. 1a, H–W model). In the "slow pressurization" limit, the fluid pressure in the initial crack is assumed to be the same as the pressure in the borehole (Fig. 1b, H–F model). Both limits are in line with the LEFM (Fig. 1c, R–W model). The duality between strength and toughness based on the interpretation of the fracture-initiation pressure has also been examined from the LEFM perspective (Lecampion, 2012). Comparing hoop stress and rock tensile strength during pressurization (H-W criterion), the prediction of wellbore pressure for fracture initiation is independent of the borehole radius. Size effects that have been observed experimentally (Carter, 1992) can only be reproduced using a non-linear model instead of LEFM. In non-linear or finite fracture mechanics (NFM), mixed criteria (stress and energy) are used to reproduce size effects. In these models, the stress singularity at the crack tip in LEFM is replaced by a cohesive/process zone in NFM. Lecampion (2012) has shown that the transition between strength-driven failure (e.g., the H-W criterion) and energy-driven failure is governed by the material length scale (the square ratio between the material fracture toughness over its tensile strength) and the structural length scale (i.e., borehole radius).

Strictly speaking, the toughness-dominated H-W model (fast limit) is only applicable in case of sleeve fracturing (Serata et al., 1992; Ishida et al., 1997; Brenne et al., 2013; Zhuang et al., 2019a). The sleeve represents the upper bound of the highly viscous fluid. Assumptions about the toughness-based interpretation (slow pressurization limit) of the fracture initiation pressure (H-F model) are its small initial flaw size, the lack of a drop-in viscosity in the crack during pressurization, and a small far-field stress deviator (Detournay and Carbonell, 1997). BP increases with increasing viscosity and injection rate (Weijers et al., 1994; Detournay and Carbonell, 1997; Lecampion et al., 2017). A high injection rate and high-viscosity injection experiments promote a dominant single fracture path of fluid (viscosity-dominated regime). A low injection rate and low viscosity promote an isotropic ring of infiltration around the borehole in case of isotropic stress (toughness-dominated regime, zero viscosity).

We summarize and explain this injection behavior through synoptic pictures indicating the infiltration zone and the generated fractures at different scenarios of low, fast, and cyclic pumping, as shown in Fig. 22a–i for an anisotropic stress state in 2D. Fluid pressure is the highest

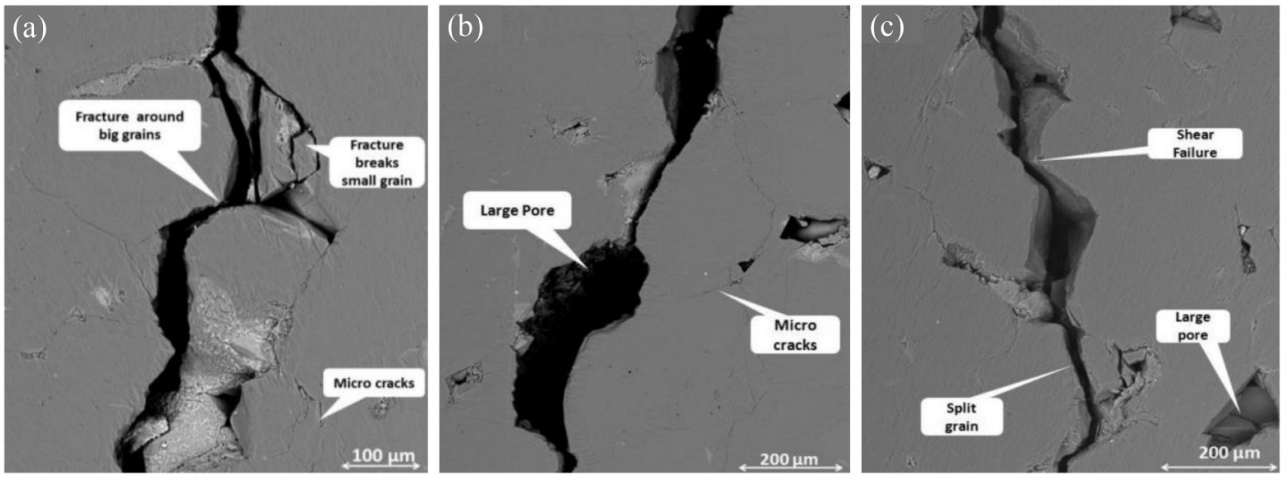

Figure 20. *SEM images of hydraulic fractures in Lyons tight sandstone: (a) Intergranular and intragranular fractures as well as cracks created adjacent to the main fracture, (b) an increase in fracture aperture due to a pore in its path, and (c) tensile (split) and shear failure. (Modified from Damani et al., 2013).*

in the borehole and is measured as injection pressure. Fluid pressure in the rock matrix decreases with increasing distance away from the borehole wall. Fast pumping (Fig. 22a) corresponds to a small infiltration ellipse (Fig. 22d), while slow pumping (Fig. 22b) creates a large infiltration ellipse (Fig. 22e). Less infiltration results in higher BP. In other words, the buildup of BP is faster for small infiltration zones. Fast pumping is best described by the H-W model with an upper bound in sleeve fracturing, and slow pumping is best described by the H-F model using permeable-rock properties (see Fig. 1). The damage zone consists of mainly tensile cracks for fast pumping, and fractures can be generated outside the infiltration zone (Fig. 22g). For slow pumping, tensile cracks are generated close to the borehole while grain-boundary fractures (i.e., hydro-shears) are generated far away from the borehole both within and outside of the infiltration zone (Fig. 22h). The tensile cracks have relatively smaller aperture and length compared with those in fast pumping due to lower injection pressure while damage zone is wider in the former. Cyclic pumping (Fig. 22i) creates the largest infiltration zone, which is engineered over several pressurization stages (e. g., Cycles 1, 2, and 3) and crack-tip relaxation stages. Cyclic damage-zone ellipses consist of both tensile fractures close to the borehole (Cycle 1) and grain-boundary fractures farther away (Cycle 2). In Cycle 3, the hydro-shear events from Cycle 2 and new shear cracks can interact with natural fractures farther away from the injection borehole. In contrast to Fig. 1 (isotropic stress field), in Fig. 22, the anisotropy of the stress field has been considered in the visualization both of the elliptical infiltration zone and of the anisotropic fracture damage zone.

A systematic quantification of the errors made by equating the BP with the H-F initiation pressure in less-than-ideal conditions (injection rate, borehole diameter, hydraulic compliance of the injection system) has been undertaken by Lakirouhani et al. (2016). The authors use a plane-strain hydraulic fracture-extension model, in which fracture initiated from the borehole and propagated into impermeable rock. The disagreement between theoretical predictions and laboratory observations in the BP can be induced by (1) the compressibility of the injection system, (2) the flow of a viscous fluid into the fracture, and (3) the far-field stress deviator. In addition, a recent study pointed out the time dependence of hydraulic fracture initiation in granite as well as other types of rock, such as limestone and sandstone, in which hydraulic fracture initiation is delayed when the borehole is pressurized under instantaneous initiation pressure, and the time delay is increased for fracturing with a higher-viscosity fluid (Lu et al., 2015, 2020). The instantaneous fluid pressure in the borehole is controlled by the injection or pressurization rate as well by the compressibility of the injection system.

8.2. Hydraulic fracture growth

In field applications, Lecampion et al. (2017) stress four critical issues of hydraulic fracture growth: fracture height, fracture reorientation, fracture network engineering, and multiple fractures. They point out that reported fracture heights based on induced seismicity are misleading in cases of fault activation (not addressed in this study). Second, fracture reorientation takes place at 5 times the borehole radius. Reorientation is not smooth but involves mixed-mode fracturing. Higher viscosity- and injection rates play a critical role in the development of near-wellbore fracture geometry. The authors used step-down tests to decide on fracture tortuosity in the near-field. Highly viscous fluids allow for less-tortuous and more- persistent fracture growth. The above-mentioned arguments are in line with the discussion in Fig. 22. Low-rate, low-viscous hydraulic fracturing promotes a ring of infiltration with a broader fracture network in the toughness-dominated regime (Fig. 22b), whereas high-

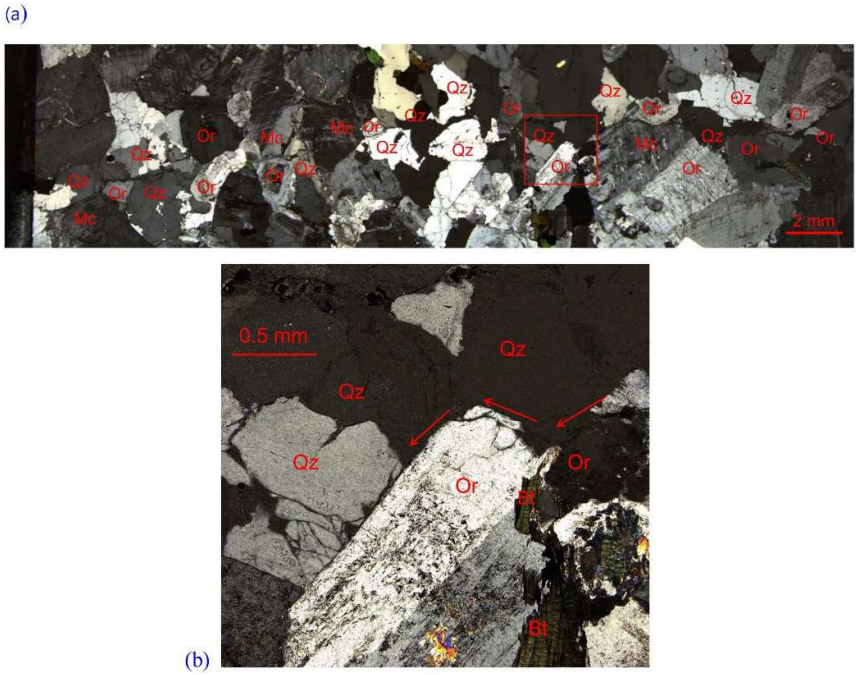

Figure 22. *Microscopic images of the thin section with mineral identification along hydraulic fractures in Pocheon granite subjected to stepwise-rate continuous injection (SCI2 specimen, Zhuang et al., 2020c): (a) Fracture at one side of borehole (SCI2-B); (b) a zoomed-in area corresponding to the box in (a). The arrows indicate fracture propagation. Qz-Quartz, Mc-Microcline, Or-Orthoclase.*

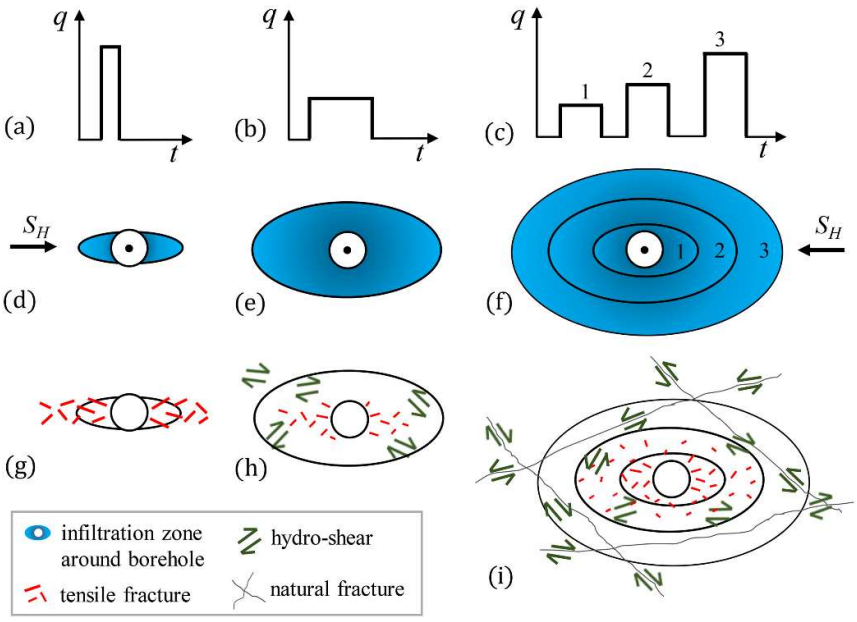

Figure 21. *Schematic diagram of fluid infiltration and damage process zones under (a) fast, (b) slow, and (c) cyclic pumping. Slow pumping creates a larger infiltration zone (e) and a larger damage zone (h) compared with those in fast pumping (d and g). For cyclic pumping, an infiltration zone (f) and an engineered fracture damage zone (i) with larger extensions can be generated in several steps. q: injection rate, t: injection time. SH refers to the maximum horizontal stress. Tensile cracks in smaller thickness and shorter length indicate less strain energy release. It should be noted that the damage- and infiltration zone can have different extensions.*

rate, high-viscosity hydraulic fractures promote dominant single fractures in the viscosity-dominated regime (Fig. 22a). The 3D fracture growth process – including appropriate coupling of fluid flow, rock deformation, and breakage – remains a challenge. Third, the authors report a larger growth of microseismic clouds with water involved in the treatment. In general, they separate localized fracture growth (isotropic stress, high viscosity, high-rate injection) from network growth (anisotropic stress, low viscosity, low-rate injection). It should be noted that in Fig. 22, both the anisotropy of the stress field and the injection rate can exert an influence on the resulting fracture pattern. Fourth, at the field scale, a horizontal well with multiple fractures at a 500-foot spacing and a 300-foot fracture height corresponds to an energy-minimized geometry for an array of simultaneously growing HFs (Bunger, 2013) because HFs avoid growing very close to one another (stress shadow effect), and HFs split the fluid among all possible fractures (fracture communication). However, the deflection of HF into regions of low stress, the growth of multiple fractures in the more stable viscosity-dominated regime, and the growth of HF from heel to toe are problems that have been addressed in numerous studies thus far, but in our opinion, they also need

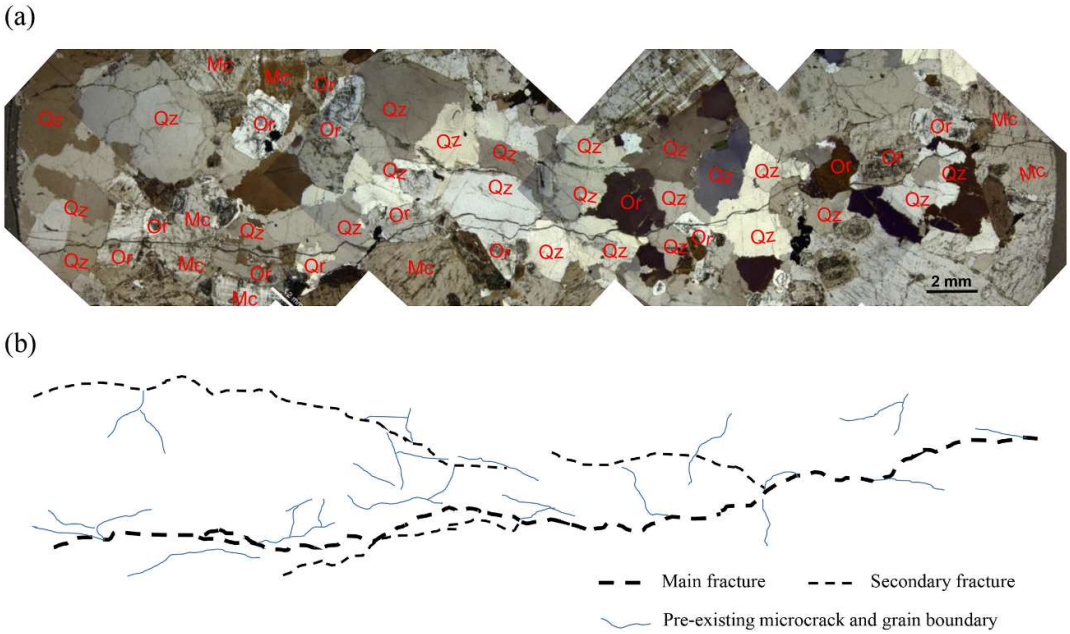

Figure 23. *Polarized light microscopy analysis result of thin section of fractured granite sample during cyclic progressive injection under true triaxial stress state. (a) Microscopic image with mineral identification along the hydraulic fracture path beginning from the borehole wall (right), Qz-Quartz, Mc-Microcline, Or-Orthoclase, (b) Line drawings of visible hydraulic fractures, pre-existing microcracks and grain boundaries.*

to be covered by experimental laboratory work.

8.3. Granite-specific hydraulic fracturing behavior

HF behavior in granite is highly dependent on minerals present, grain size and heterogeneity and is quite different from the behavior that previously observed in sedimentary rock, such as sandstone. The two types of rock are formed under different geological conditions. Sandstone is usually composed of a single kind of sand-sized silicate grains (around 0.075–2 mm according to the Unified Soil Classification System). During diagenesis, the silica grains are bonded together (e.g., calcite cement) to form a two-mineral system. While most granite is typically composed of quartz, feldspar, plagioclase, and other minor minerals, these minerals have different physical properties and strengths. Grain size and mineral distribution vary for different types of granite, which increases the difficulty in predicting hydraulic fracture propagation. On the other hand, the mineral compositions enable HF patterns to be more sensitive to test conditions, particularly to injection schemes.

Fig. 23 shows an example of a polarized light microscopy analysis result of hydraulic fractures in a Pocheon granite sample fractured during cyclic progressive injection. One main fracture and secondary fractures were generated and connected to pre-existing microcracks and grain boundaries. The results further show the advantage of cyclic injection in creating fracture networks (refer to Fig. 11), which benefit heat extraction in geothermal reservoirs.

Previous studies have pointed out different acoustic-emission behavior in granite and sandstone that has been subjected to triaxial loading. In granite, more localized failure and more AEs with higher energy (shear fracturing) are observed. In sandstone, less localized failure is documented in the broader process zone (such as shear enhanced compaction), and fewer and weaker AEs are observed due to pore collapse and porosity-related fracturing (Zang et al., 2002). Moreover, from a theoretical perspective, fracture mechanical models use pore cracks as failure sources in sandstone (Sammis and Ashby, 1986), while wing cracks are used to provide a better understanding of compressive failure in granite (Ashby and Hallam, 1986). Similar source models need to be developed for hydro-fracturing and hydro-shearing sources in fluid-injection tests. Detailed studies on AE source analysis are also required in fluid-injection experiments to shed light on the underlying microfracturing and crack-interaction mechanisms when highly pressurized fluid is involved in the failure process.

8.4. Field demonstration of cyclic stimulation

Cyclic injection has been used for stimulation in oil reservoirs to improve recovery rates (Kiel, 1977), whereas in EGS, very few cases (e. g., the progressive cyclic injection experiments at the Soultz EGS site and at GtLa2 at Landau) have been reported (Schill et al., 2017). For the experiments in the GPK1 well of the Soultz EGS site, the injection rate was stepped from 12 L/s to 36 L/s in four cycles, and shut-in intervals (a few hours) between every two cycles led to a decrease in wellhead pressure by a maximum of 7 MPa. Zimmermann et al. (2010) presented the results of cyclic waterfrac stimulation at the Groß Schönebeck EGS site for research purposes. Cyclic

stimulation that combined the use of gel proppant successfully increased the overall productivity of the treated well by four times, with moment magnitudes of associated induced seismicity events ranging from -1.8 to -1.0. Cyclic soft stimulation, the essence of which involves the combination of a cyclic fluid-injection scheme with a tailor-made seismic traffic-light system and limited injection pressure, pressurization rates, and injected net volumes was tested at the Pohang EGS site for the first time in August 2017 (Hofmann et al., 2018, 2019). During the cyclic stimulation, a seismic event with a maximum of *M*w 1.9 occurred, which was below the previously set threshold of 2.0 following the traffic-light system. However, longer-term behavior was difficult to assess since multiple stimulation treatments and other site operations had been performed before and after the CSS test at Pohang EGS (Hofmann et al., 2018). Another demonstration of the CSS was conducted in a basalt and gabbro formation on the Geldinganes peninsula in the city of Reykjavik in October 2019 (Broccardo et al., 2020). Isolated zones of the RV-43 well were stimulated with a cyclic injection scheme, which repeated every 24 hours and included pressurizing with pulses at a frequency of 1/60 Hz and continuous injection phases. Additionally, the advanced traffic-light-system (Hofmann et al., 2019) procedures were applied for the first time in this field test.

9. Conclusions

Hydraulic fracturing has wide applications in different geological conditions for energy extraction and storage as well as in in-situ stress measurements. For the purpose of applications in EGS and in-situ stress measurement, extensive experimental study of the hydraulic fracturing of granitic rock was conducted combined with advanced AE monitoring and fracture-observation methods. Significant progress was achieved in providing a better understanding of the hydraulic fracturing behavior of granitic rock. The main results are highlighted below:

(1) Simple BP models for impermeable rock (H-W model), permeable rock (H-F model), and fracture mechanical approaches (R-W model) are valuable elements in the discussion and interpretation of fluid-injection experiments on granitic rock.

(2) BP in laboratory hydraulic fracturing decreases with an increasing diameter of the injection borehole for ~20-mm-diameter boreholes, and the tensile strength of rock and stress deviators play a key role. In granitic rock with a small grain size compared with the borehole diameter, process-zone-formed tensile cracks ahead of a hydraulic fracture were found to be the underlying mechanism. For large-grain rock, localized hydro-shear along grain boundary became more likely instead of tensile cracks. Preferred mineral orientation (foliation) also plays a role. Splitting is easier when the injected water runs parallel to the foliation.

(3) Above a temperature of 300°C, BP is reduced significantly (at a range of 20%–40%) due to thermal cracking in granite and to leak-off. More cracks are induced at breakdown in saturated granite compared with dry granite. Pre-existing flaws can propagate in Mode I and/or Mode II, and well below the least principal stress. Coalescing fractures can enhance permeability well above those of rock with isolated pre-existing flaws.

(4) Low-viscous fluid induces shear-dominant fractures, whereas highly viscous fluid induces tensile-dominant fractures. BP increases with increasing viscosity of injection fluid when the other test conditions are the same. The infiltration of fluid is largely influenced by fluid viscosity and discontinuities in rock. A threshold injection rate exists for increasing the BP under certain stress conditions. HF opens in the direction of least principal stress and rapidly propagates in the plane containing the largest and intermediate principal stress. The rate of HF propagation decreases with an increase in the least principal stress. Process-zone-related cracks narrow as the principal stress ratio increases.

(5) Fatigue hydraulic fracturing is a promising and innovative injection scheme that uses cyclic and pulse pressurization because low and high injection pressure cycles have the potential to lower BP, and pressure pulse oscillations have the potential to generate natural proppants. In the hydraulic fatigue concept, rock chips removed from fracture wall through pressure oscillations can change the local crack-tip stress field and allow a broader damage zone to be engineered. Optimization potential remains when it comes to finding a fluid-injection scheme that minimizes the seismic-energy-release rate.

(6) AE monitoring and CT as non-destructive techniques allow for independent information on fracture characteristics to be ascertained. AE allows for gaining extra information on the radiated seismic energy, and CT allows for gaining information on the fracture surface energy. While the AE hypocenter can trace fractures and provide source information, CT image analysis allows fracture geometries to be quantitatively analyzed in detail. A combination of AE and CT allows the respective relationship between seismic clouds and actual fracture networks to be calibrated, which helps in estimating the stimulated reservoir volume. Microscopic observations allow quantitative evaluation on fractures and minerals along the fracture, which provides a better understanding of hydraulic fracturing mechanism.

(7) The H-W model stands for the case of HF in impermeable rock (i.e., sleeve fracturing), which is characterized by fast-pumping, highly viscous fluid and a high BP due to the negligible infiltration zone. The H-F model, on the other hand, can be used by

interpreting the situation in permeable rock characterized by slow-pumping, low-viscous fluid and a relatively lower buildup of BP in a relatively larger infiltration zone. As an innovative new technique, cyclic pumping combined with pulse pressurization has the potential to engineer the largest process zone via crack-tip relaxation and to form natural proppants.

(8) We noted the different hydraulic fracturing behavior in granite compared with that in sandstone, emphasizing that HFs in granite are mineral composition dependent. The impact of BP reduction by cyclic and pulse pressurization is more pronounced in hard rock (granite) compared with soft rock (sandstone). The fluid-injection-induced fracturing mechanism in sandstone may be vastly different from that in granite. While pore collapse and pore-interaction processes can play a role in sandstone, in granite, mineral-specific intra- and inter-granular (grain boundary) fracturing events can play a role. These source events have an impact on the damage zone and on permeability evolution in fluid-injection experiments.

We recommend that future studies focus on the role of natural proppants and the leak-off process in hydraulic fatigue. Cyclic stimulation in the field requires proper managing of optimized injection parameters, including high-pressure oscillations, for successful and sustainable permeability enhancement. The hydraulic fatigue fragmentation process, like any other stimulation treatment, also has limitations when hydraulic fractures begin to interact with pre-existing faults and runaway tectonic fractures are triggered. The growth of multiple fractures in the viscosity-dominated regime, the shearing of pre-existing fractures, and mixed-mode fracture processes as well as the pressure distribution inside the fractures need to be addressed and covered in future laboratory experiments.

Declaration of Competing Interest

No conflict of interest was reported by the authors.

Acknowledgements

This work was supported by the International Collaborative Research Program (20170515-001, 20180583-001, 20190282-001, 20200209- 001) funded by Korea Institute of Civil Engineering and Building Technology (KICT). The authors are grateful for the funding received from the European Commission Horizon 2020 research and innovation program under grant agreement No. 691728 (DESTRESS). We wish to thank Sun Yeom in KICT for conducting CT image processing.

References

Adachi, J., Siebrits, E., Peirce, A., Desroches, J., 2007. Computer simulation of hydraulic fractures. Int. J. Rock Mech. Min. Sci. 44 (1), 739–757.

Amadei, B., Stephansson, O., 1997. Rock stress and its measurement. Chapman & Hall, London, p. 478.

Ashby, M.F., Hallam, S.D., 1986. The failure of brittle solids containing small cracks under compressive stress states. Acta Metall. 34 (3), 497–510.

ASTM, 2011. E1441-11 Standard guide for computed tomography (CT) imaging. American Society for Testing and Materials, West Conshohocken, PA.

Bai, J., Martysevich, V., Walters, H., Dusterhoft, R., Matzar, L., Sansil, M., 2016. Laboratory-scale hydraulic fracturing: experiment and numerical modeling. The 50th US Rock Mechanics /Geomechanics Symposium. American Rock Mechanics Association, Houston, ARMA, pp. 16–123.

Bao, X., Eaton, D.W., 2016. Fault activation by hydraulic fracturing in western Canada. Science 354 (6318), 1406–1409.

Baptista-Pereira, C., Li, B., Gonçalves Silva, B., 2020. Time- and pressure-dependent source mechanisms in hydraulic fracturing tests in granite considering fluid diffusivity. In: The 54th US Rock Mechanics /Geomechanics Symposium. American Rock Mechanics Association, Golden. ARMA 2020-1587.

Bauer, S., Huang, K., Chen, Q., Ghassemi, A., Barrow, P., 2016. Experimental and numerical investigation of hydro-thermally induced shear stimulation. In: The 50th US Rock Mechanics/Geomechanics Symposium, American Rock Mechanics Association, Houston, ARMA 2016-257.

Belyadi, H., Fathi, E., Belyadi, F., 2019. Numerical simulation of hydraulic fracturing propagation. In: Hydraulic Fracturing in Unconventional Reservoirs, 2nd ed. Theories, Operations, and Economic Analysis, pp. 257–272.

Blanton, T.L., 1982. An experimental study of interaction between hydraulically induced and preexisting fractures. In: The SPE/DOE Unconventional Gas Recovery Syrup, Pittsburgh, PA. Paper SPE10847.

Blanton, T.L., 1986. Propagation of hydraulically and dynamically induced fractures in naturally fractured reservoirs. Soc. Pet. Eng. J. 613–621 https://doi.org/10.2118/ 15261-MS.

Bradford, J., Ohren, M., Osborn, W.L., McLennan, J., Moore, J., Podgorney, R., 2014. Thermal stimulation and injectivity testing at Raft River, ID EGS site. In: The 39th Workshop on Geothermal Reservoir Engineering, Stanford, California. Breede, K., Dzebisashvili, K., Liu, X., Falcone, G., 2013. A systematic review of enhanced (or engineered) geothermal systems: past, present and future. Geotherm. Energy 1, 4.

Brenne, S., Molenda, M., Stoeckhert, F., Alber, M., 2013. Hydraulic and sleeve fracturing laboratory experiments on 6 rock types. https://doi.org/10.5772/56301.

Broccardo, M., Mignan, A., Karvounis, D., Rinaldi, A.P., Danciu, L., Hofmann, H., Mikereit, C., Dahm, T., Zimmermann, G., Hjörleifsdóttir, V., Wiemer, S., 2020. Induced seismicity risk analysis of the hydraulic stimulation of a geothermal well on Geldinganes, Iceland. Nat. Hazards Earth Syst. Sci. 20, 1573–1593.

Brown, D.W., Duchane, D.V., 1999. Scientific progress on the Fenton Hill HDR project since 1983. Geothermics 28, 591–601.

Bunger, A., Lecampion, B., 2017. Four critical issues for successful hydraulic fracturing applications. In: Rock Mechanics and Engineering, 5. CRC Press, Balkema (Surface and Underground Projects), Chapter 16.

Bunger, A.P., 2013. Analysis of the power input needed to propagate multiple hydraulic fractures. Int. J. Solids Struct. 50, 1538–1549.

Bunger, A.P., Detournay, E., Garagash, D.I., 2005. Toughness-dominated hydraulic fracture with leak-off. Int. J. Fract. 134, 175–190.

Cacas, L.A., 2005. Large scale hydraulic fracturing test on a rock with artificial discontinuities. Master's thesis. Colorado School of Mines, Golden, Colorado.

Carter, B.J., 1992. Size and stress gradient effects on fracture around cavities. Rock Mech. Rock. Eng. 25 (3), 167–186.

Chang, S.H., Lee, C.I., 2004. Estimation of cracking and damage mechanisms in rock under triaxial compression by moment tensor analysis of acoustic emission. Int. J. Rock Mech. Min. Sci. 41 (7), 1069–1086.

Chen, Y., Nagaya, Y., Ishida, T., 2015. Observations of fractures induced by hydraulic fracturing in anisotropic granite. Rock Mech. Rock. Eng. 48, 1455–1461.

Cheng, W., Jin, Y., Chen, M., 2015. Experimental study of step-displacement hydraulic fracturing on naturally fractured shale outcrops. J.

Geophys. Eng. 12, 714–723.
Chitrala, Y., Sondergeld, C., Rai, C., 2012. Acoustic emission studies of hydraulic fracture evolution using different fluid viscosities. In: The 46th US rock mechanics/ geomechanics symposium. Chicago, 24-27 June, ARMA 12-597.
Chitrala, Y., Moreno, C., Sondergeld, C., Rai, C., 2013. An experimental investigation into hydraulic fracture propagation under different applied stresses in tight sands using acoustic emissions. J. Pet. Sci. Eng. 108, 151–161.
Cnudde, V., Boone, M.N., 2013. High-resolution X-ray computed tomography in geosciences: A review of the current technology and applications. Earth-Sci. Rev. 123, 1–17.
Cordero, Z.C., Knight, B.E., Schuh, C.A., 2016. Six decades of the Hall-Petch effect – a survey of grain-size strengthening studies on pure metals. Int. Mater. Rev. 61 (8), 495–512.
Cornet, F., Bérard, T., Bourouis, S., 2007. How close to failure is a granite rock mass at a 5 km depth? Int. J. Rock Mech. Min. Sci. 44 (1), 47–66.
Cornet, F.H., 2021. The engineering of safe hydraulic stimulations for EGS development in hot crystalline rock masses. Geomech. Energy Envir. 26, 100151. https://doi.org/ 10.1016/j.gete.2019.100151.
Damani, A., Sharma, A., Sondergeld, C.H., Rai, C.S., 2013. Acoustic mapping and microscopic analysis of laboratory Induced hydraulic fractures under triaxial stress conditions. In: The 47th US Rock Mechanics/Geomechanics Symposium, Minneapolis, Minnesota, ARMA 13-586.
Davies, R., Foulger, G., Bindley, A., Styles, P., 2013. Induced seismicity and hydraulic fracturing for the recovery of hydrocarbons. Mar. Pet. Geol. 45, 171–185.
Degue, K.M., Ladanyi, B., 2000. Effect of fluid penetration and pressurizing rate on hydraulic fracturing. In: Girard, Liebman, Breeds & Doe (Eds.), Pacific Rocks 2000. Balkema, Rotterdam, pp. 181–188.
Dehghan, A.N., Goshtasbi, K., Ahangari, K., Jin, Y., 2016. Mechanism of fracture initiation and propagation using a triaxial hydraulic fracturing test system in naturally fractured reservoirs. Eur. J. Environ. Civ. Eng. 20 (5), 560–585.
Detournay, E., 2004. Propagation regimes of fluid-driven fractures in impermeable rocks. Int. J. Geomech. 4 (1), 1–11.
Detournay, E., 2016. Mechanics of hydraulic fractures. Annu. Rev. Fluid Mech. 48, 311–339.
Detournay, E., Carbonell, R., 1997. Fracture-mechanics analysis of the breakdown process in minifracture or leakoff test. SPE Product. Facilit. 12 (3), 195–199.
Detournay, E., Cheng, A., 1992. Influence of pressurization rate on the magnitude of the breakdown pressure. In: Tillerson & Wawersik (Eds.). Rock Mechanics, Balkema, Rotterdam.
Detournay, E., Cheng, A., 1993. Comprehensive rock engineering: Principles, practice and projects. In: Hudson, J.A. (Ed.), Fundamentals of Poroelasticity. Pergamon Press, Oxford, pp. 113–171.
Detournay, E., Peirce, A.P., Bunger, A.P., 2007. Viscosity-dominated hydraulic fractures. In: The 1st Canada - U.S. Rock Mechanics Symposium, 27-31 May, Vancouver, ARMA-07-205.
Diaz, M., Jung, S.G., Zhuang, L., Kim, K.Y., Jung, J.H., Shin, H.S., 2016a. Tensile strength anisotropy of Pocheon granite and roughness evaluation of its failure planes. In: Ulusay et al. (Eds.) Rock Mechanics and Rock Engineering: From the Past to the Future (EUROCK 2016). Taylor & Francis Group, London.
Diaz, M., Jung, S.G., Zhuang, L., Kim, K.Y., Yeom, S., Shin, H.S., 2016b. Effect of cleavage anisotropy on hydraulic fracturing behavior of Pocheon grantie. In: The 50th US Rock Mechanics / Geomechanics Symposium, Houston, ARMA 16-143.
Diaz, M., Jung, S.G., Zhuang, L., Kim, K.Y., 2018a. Comparison of acoustic emission activity in conventional and cyclic hydraulic fracturing in cubic granite samples under triaxial stress state. In: The 52nd US Rock Mechanics/Geomechanics Symposium. Seattle, ARMA 18–1160.
Diaz, M., Jung, S.G., Zhuang, L., Kim, K.Y., Zimmermann, G., Hofmann, H., Zang, A., Stephansson, O., Min, K.B., 2018b. Hydraulic, mechanical and seismic observations during hydraulic fracturing by cyclic injection on Pocheon granite. In: The 10th Asian Rock Mechanics Symposium, Oct 29- Nov 3, Singapore.
Diaz, M., Jung, S.G., Zhuang, L., Kim, K.Y., Hofmann, H., Min, K.B., Zang, A., Zimmermann, G., Stephansson, O., Yoon, J.S., 2018c. Laboratory investigation of hydraulic fracturing of granite under true triaxial stress state using different injection schemes – Part 2. Induced seismicity. In: International Conference on Coupled Processes in Fractured Geological Media: Observation, Modeling, and Application, Wuhan.
Douglass, P.M., Voight, B., 1969. Anisotropy of granites: a reflection of microscopic fabric. Geotechnique 19, 376–398.
Duevel, B., Haimson, B., 1997. Mechanical characterization of pink Lac Du Bonnet granite: evidence of nonlinearity and anisotropy. Int. J. Rock Mech. Min. Sci. 34 (3- 4). Paper No. 117.
Dutler, N., Valley, B., Gischig, V., Villiger, L., Krietsch, H., Doetsch, J., Brixel, B., Jalali, M., Amann, F., 2019. Hydraulic fracture propagation in a heterogeneous stress field in a crystalline rock mass. Solid Earth 10, 1877–1904.
Eberhardt, E., Stimpson, B., Stead, D., 1999. Effects of grain size on the initiation and propagation thresholds of stress-induced brittle fracture. Rock Mech. Rock. Eng. 32 (2), 81–99.
Economides, M.J., Nolte, K.G., 2000. Reservoir Stimulation, 3rd ed. John Wiley & Sons, New York.
Evans, K.F., Zappone, A., Kraft, T., Deichmann, N., Moia, F., 2012. A survey of the induced seismic responses to fluid injection in geothermal and CO2 reservoirs in Europe. Geothermics 41, 30–54.
Fairhurst, C., 1964. Measurement of in situ rock stresses with particular references to hydraulic fracturing. Rock Mech. Eng. Geol. 2, 129–147.
Fallahzadeh, S.H., Hossain, M., Cornwell, A., Rasouli, V., 2017. Near wellbore hydraulic fracture propagation from perforations in tight rocks: the roles of fracturing fluid viscosity and injection rate. Energies 10, 359. https://doi.org/10.3390/en10030359.
Fan, T., Zhang, G., 2014. Laboratory investigation of hydraulic fracture networks in formations with continuous orthogonal fractures. Energy 74, 164–173.
Fatahi, H., Hossain, M.M., Sarmadivaleh, M., 2017. Numerical and experimental investigation of the interaction of natural and propagated hydraulic fracture. J. Nat. Gas Sci. Eng. 37, 409–424.
Frash, L.P., 2014. Laboratory scale study of hydraulic fracturing in heterogeneous media for enhanced geothermal systems and general well stimulation. Doctoral Thesis. Colorado School of Mines, Golden, Colorado.
Frash, L.P., Gutierrez, M., Hampton, J., Hood, J., 2015. Laboratory simulation of a binary and triple well EGS in large granite blocks using AE events for drilling guidance. Geothermics 55, 1–15.
Frash, L.P., Carey, J.W., Viswanathan, H.S., 2016. Notched specimen hydraulic fracturing method for conducting mechanical and hydrological experiments at triaxial reservoir conditions. In: The 50th US Rock Mechanics / Geomechanics Symposium, Houston, ARMA 16-503.
Fu, P., Settgast, R.R., Hao, Y., Morris, J.P., Ryerson, F.J., 2017. The influence of hydraulic fracturing on carbon storage performance. J. Geophys. Res. Solid Earth 122, 9931–9949.
Gandossi, L., 2013. An overview of hydraulic fracturing and other formation stimulation technologies for shale gas production. In: Technical report, Joint Research Center, Institute for Energy and Transport.
Garagash, D., Detournay, E., 1996. Influence of pressurization rate on borehole breakdown pressure in impermeable rocks. In: Aubertin, Hassani & Mitri (Eds), Rock Mechanics. Balkema, Rotterdam.
Garagash, D.I., Detournay, E., 2002. Viscosity-dominated regime of a fluid-driven fracture in an elastic medium. In: Karihaloo, B.L. (Ed.), Solid Mechanics and Its Applications, proceedings of IUTAM Symposium on Analytical and Computational Fracture Mechanics of Non-Homogeneous Materials, 97. Springer, Dordrecht.
Ghassemi, A., 2012. A review of some rock mechanics issues in geothermal reservoir development. Geotech. Geol. Eng. 30, 647–664. Giardini, D., 2009. Geothermal quake risks must be faced. Nature 462, 848–849.
Gischig, V.S., Preisig, G., 2015. Hydro-fracturing versus hydro-shearing: a critical assessment of two distinct reservoir stimulation mechanisms. In: The 13th International Congress of Rock Mechanics, 10-13 May, Montréal.
Gonçalves Silva, B., Einstein, H., 2018. Physical processes involved in the laboratory hydraulic fracturing of granite: Visual observations and interpretation. Eng. Fract. Mech. 191, 125–142.
Goodfellow, S., Nasseri, M.H.B., Young, R.P., 2013. The influence of injection rate on hydraulic fracturing of tri-axially deformed Westerly granite. In: The 47th US Rock Mechanics / Geomechanics Symposium, San Francisco, ARMA 13-543.
Goodfellow, S.D., Nasseri, M.H.B., Maxwell, S.C., Young, R.P., 2015.

Hydraulic fracture energy budget: Insights from the laboratory. Geophys. Res. Lett. 42, 3179–3187.
Goodfellow, S.D., Lee, B., Flynn, W., Maxwell, S.C., Nasseri, M.H.B., Young, R.P., Lombos, L.E.A., 2016. Acoustic emission geomechanics of hydraulic fracturing in the laboratory. In: The 50th US Rock Mechanics / Geomechanics Symposium, Houston, ARMA 16-524.
Groenenboom, J., van Dam, D.B., 2000. Monitoring hydraulic fracture growth: Laboratory experiments. Geophysics 65 (2), 603–611.
Guo, F., Morgenstern, N.R., Scott, J.D., 1993a. Interpretation of hydraulic fracturing breakdown pressure. Int. J. Rock Mech. Min. Sci. Geomech. Abstr. 30 (6), 617–626.
Guo, F., Morgenstern, N.R., Scott, J.D., 1993b. An experimental investigation into hydraulic fracture propagation - Part 1. Experimental facilities. Int. J. Rock Mech. Min. Sci. Geomech. Abstr. 30 (3), 177–188.
Guo, F., Morgenstern, N.R., Scott, J.D., 1993c. An experimental investigation into hydraulic fracture propagation - Part 2. Single well tests. Int. J. Rock Mech. Min. Sci. Geomech. Abstr. 30 (3), 189–202.
Ha, S.J., Yun, T.S., 2020. Experimental and numerical investigation of time-delayed pressurization for the manipulation of breakdown pressure and acoustic emissions during hydraulic stimulation. Eng. Fract. Mech. 231, 107005.
Ha, S.J., Yun, T.S., Kim, K.Y., Jung, S.G., 2017. Experimental study of pumping rate effect on hydraulic fracturing of cement paste and mortar. Rock Mech. Rock. Eng. 50, 3115–3119.
Haimson, B., 1968. Hydraulic fracturing in porous and nonporous rock and its potential for determining in situ stresses at great depth. Ph.D. Thesis. University of Minnesota, U.S.A.
Haimson, B., Fairhurst, C., 1967. Initiation and extension of hydraulic fractures in rocks. Soc. Pet. Eng. J. 7, 310–318.
Haimson, B., Fairhurst, C., 1969. Hydraulic fracturing in porous-permeable materials. J. Pet. Technol. 811–817. July.
Haimson, B., Zhao, Z., 1991. Effect of borehole size and pressurization rate on hydraulic fracturing breakdown pressure. In: Roegiers, J.C. (Ed.), Rock Mechanics as a Multidisciplinary Science. Balkema, Rotterdam, pp. 191–199.
Hampton, J., Hu, D., Matzar, L., Gutierrez, M., 2014. Cumulative volumetric deformation of a hydraulic fracture using acoustic emission and micro-CT imaging. In: The 48th US Rock Mechanics / Geomechanics Symposium, Minneapolis, ARMA 14-7041.
Hampton, J., Gutierrez, M., Frash, L., 2019. Predictions of macro-scale fracture geometries from acoustic emission point cloud data in a hydraulic fracturing experiment. J. Petrol. Explor. Prod. Tech. 9, 1175–1184.
Hampton, J., Gutierrez, M., Matzar, L., Hu, D., Frash, L., 2018. Acoustic emission characterization of microcracking in laboratory-scale hydraulic fracturing tests. J. Rock Mech. Geotech. Eng. 805–817.
Hartman, W.F., 1977. Towards standards for acoustic emission technology. In: Berger, H. (Ed.), Nondestructive Testing Standards—A Review. ASTM International, West Conshohocken, PA, pp. 138–145.
Hashiba, K., Fukui, K., 2015. Effect of water on the deformation and failure of rock in uniaxial tension. Rock Mech. Rock. Eng. 48, 1751–1761.
Hassebroek, W.E., Waters, A.B., 1964. Advances through 15 years of fracturing. J. Pet. Technol. 16 (7), 760–764.
He, J., Lin, C., Li, X., Wan, X., 2016. Experimental investigation of crack extension patterns in hydraulic fracturing with shale, sandstone and granite cores. Energies 9, 1018. https://doi.org/10.3390/en9121018.
Heuze, F.E., 1983. High-temperature mechanical, physical and Thermal properties of granitic rocks—a review. Int. J. Rock Mech. Min. Sci. Geomech. Abstr. 20, 3–10.
Hofmann, H., Zimmermann, G., Zang, A., Min, K.B., 2018. Cyclic soft stimulation (CSS): a new fluid injection protocol and traffic light system to mitigate seismic risks of hydraulic stimulation treatments. Geotherm. Energy 6, 27.
Hofmann, H., Zimmermann, G., Farkas, M., Huenges, E., Zang, A., Leonhardt, M., Kwiatek, G., Martinez-Garzon, P., Bohnhoff, M., Min, K.B., Fokker, P., Westaway, R., Bethmann, F., Meier, P., Yoon, K.S., Choi, J.W., Lee, T.J., Kim, K.Y., 2019. First field application of cyclic soft stimulation at the Pohang Enhanced Geothermal System site in Korea. Geophys. J. Int. 217, 926–949.
Hu, L., Ghassemi, A., Pritchett, J., Garg, S., 2016. Laboratory scale investigation of enhanced geothermal reservoir stimulation. In: The 41st Workshop on Geothermal Reservoir Engineering, Stanford, California, SGP-TR-209.
Hu, L., Ghassemi, A., Pritchett, J., Garg, S., 2017. Experimental investigation of hydraulically induced fracture properties in enhanced geothermal reservoir stimulation. In: The 42nd Workshop on Geothermal Reservoir Engineering, Stanford, California, SGP-TR-212.
Hu, L., Ghassemi, A., Riley, S., Kahn, D., 2019. Lab-scale experiments investigating the possibility of bedding plane slip events during microseismic monitoring of hydraulic fracturing. In: The 53rd US Rock Mechanics/Geomechanics Symposium, New York, ARMA 2019-1870.
Huang, B., Liu, J., 2017. Experimental investigation of the effect of bedding planes on hydraulic fracturing under true triaxial stress. Rock Mech. Rock. Eng. 50, 2627–2643.
Huang, K., Cheng, Q., Ghassemi, A., Bauer, S., 2019. Investigation of shear slip in hot fractured rock. Int. J. Rock Mech. Min. Sci. 120, 68–81.
Hubbert, K.M., Willis, D.G., 1957. Mechanics of hydraulic fracturing. Petrol. Trans. AIME 210, 153–168.
Ishibashi, T., Asanuma, H., Ishikawa, S., Watanabe, N., 2018. Concurrent monitoring of hydraulic and mechanical properties of granite fracture during hydraulically induced shearing in laboratory. In: The 52nd U.S. Rock Mechanics/Geomechanics Symposium. Seattle, ARMA 18–369.
Ishida, T., 2001. Acoustic emission monitoring of hydraulic fracturing in laboratory and field. Constr. Build. Mater. 15, 283–295.
Ishida, T., Chen, Q., Mizuta, Y., 1997. Effect of injected water on hydraulic fracturing deduced from acoustic emission monitoring. Pure Appl. Geophys. 150, 627–646.
Ishida, T., Sasaki, S., Matsunaga, I., Chen, Q., Mizuta, Y., 2000. Effect of grain size in granitic rocks on hydraulic fracturing mechanism. In: Trends in Rock Mechanics, Geotechnical Special Publication No.102, ASCE, pp. 128–139.
Ishida, T., Chen, Q., Mizuta, Y., Roegiers, J.C., 2004. Influence of fluid viscosity on the hydraulic fracturing mechanism. J. Energ. Resour-ASME. 126, 190–200.
Ishida, T., Aoyagi, K., Niwa, T., Chen, Y., Murata, S., Chen, Q., Nakayama, Y., 2012. Acoustic emission monitoring of hydraulic fracturing laboratory experiment with supercritical and liquid CO2. Geophys. Res. Lett. 39 (16), 1–6.
Ishida, T., Chen, Y., Bennour, Z., Yamashita, H., Inui, S., Nagaya, Y., Naoi, M., Chen, Q., Nakayama, Y., Nagano, Y., 2016. Features of CO2 fracturing deduced from acoustic emission and microscopy in laboratory experiments. J. Geophys. Res. Solid Earth 121, 8080–8098.
Ishida, T., Labuz, J.F., Manthei, G., Meredith, P.G., Nasseri, M.H.B., Shin, K., Yokoyama, T., Zang, A., 2017. ISRM suggested method for laboratory acoustic emission monitoring. Rock Mech. Rock. Eng. 50 (3), 665–674.
Ito, T., Hayashi, K., 1991. Physical background to the breakdown pressure in hydraulic fracturing tectonic stress measurement. Int. J. Rock Mech. Min. Sci. Geomech. Abstr. 28 (4), 285–293.
Ji, Y., Wu, W., 2018. Overpressure-induced fractional slip of rock fractures. In: The 10th Asian Rock Mechanics Symposium, Oct 29- Nov 3, Singapore. Ji, Y., Wu, W., 2020. Injection-driven fracture activation in granite: mechanism and implications. Tectonophysics 791, 228572.
Ji, Y., Wanniarachchi, W.A.M., Wu, W., 2020. Effect of fluid pressure heterogeneity on injection-induced fracture activation. Comput. Geotech. 123, 103589.
Ji, Y., Zhuang, L., Wu, W., Hofmann, H., Zang, A., Zimmermann, G., 2021. Cyclic water injection potentially mitigates seismic risks by promoting slow and stable slip of a natural fracture in granite. Springer. Manuscript submitted for publication.
Ju, Y., Xi, C., Zhang, Y., Mao, L., Gao, F., Xie, H., 2018. Laboratory in situ CT observation of the evolution of 3D fracture networks in coal subjected to confining pressures and axial compressive loads: a novel approach. Rock Mech. Rock. Eng. 51, 3361–3375.
Jung, S.G., Diaz, M., Zhuang, L., Kim, K.Y., Shin, H.S., Jung, J.H., 2016. Influence of injection rate and viscosity on hydraulic fracturing behaviour of granite. In: The 9th Asian Rock Mechanics Symposium, October 18-20, Bali.
Kahraman, S., 2007. The correlations between the saturated and dry P-wave velocity of rocks. Ultrasonics 46 (4), 341–348.
Ketcham, R.A., Carlson, W.D., 2001. Acquistion, optimization and interpretation of X-ray computed tomographic imagery: applications to the geosciences. Comput. Geosci. 27, 381–400.
Kiel, O.M., 1977. The Kiel process - reservoir stimulation by dendritic fracturing. Tech. Rep., Society of Petroleum Engineers, SPE-6984.

Kizaki, A., Tanaka, H., Sakaguchi, K., 2013. Hydraulic fracturing in Inada granite and Ogino tuff using super critical carbon dioxide and water as fracturing fluids. J. Min. Mater. Proc. Inst. Jpn. 129, 461–466 (in Japanese).

Kovalyshen, Y., Detournay, E., 2009. A reexamination of the classical PKN model of hydraulic fracture. Transport Porous Med. 81 (2), 317–339.

Kovalyshen, Y., Bunger, A.P., Kear, J., Kasperczyk, D., 2014. Comparison between ultrasonic and photometric methods for hydraulic fracturing laboratory monitoring. Int. J. Rock Mech. Min. Sci. 70, 368–374.

Kumari, W.G.P., Ranjith, P.G., Perera, M.S.A., Li, X., Li, L.H., Chen, B.K., Isaka, B.L.A., De Silva, V.R.S., 2018. Hydraulic fracturing under high temperature and pressure conditions with micro CT applications: geothermal energy from hot dry rocks. Fuel 230, 138–154.

Kwiatek, G., Charalampidou, E.-M., Dresen, G., Stanchits, S., 2014. An improved method for seismic moment tensor inversion of acoustic emissions through assessment of sensor coupling and sensitivity to incidence angle. Int. J. Rock Mech. Min. Sci. 65, 153–161. https://doi.org/10.1016/j.ijrmms.2013.11.005.

Labuz, J., Zang, A., 2012. Mohr-Coulomb failure criterion. Rock Mech. Rock. Eng. 45 (6), 975–979.

Lajtai, E., Schmidtke, R., Bielus, L., 1987. The effect of water on the time-dependent deformation and fracture of a granite. Int. J. Rock Mech. Min. Sci. Geomech. Abstr. 24, 247–255.

Lakirouhani, A., Detournay, E., Bunger, A.P., 2016. A reassessment of in situ stress determination by hydraulic fracturing. Geophys. J. Int. 205, 1859–1873.

Lau, J.S.O., Chandler, N.A., 2004. Innovative laboratory testing. Innov. Lab. Test. 41 (8),

Lecampion, B., 2012. Modeling size effects associated with tensile fracture initiation from a wellbore. Int. J. Rock Mech. Min. Sci. 56, 67–76.

Lecampion, B., Desroches, J., Jeffrey, R.G., Bunger, A.P., 2017. Experiments versus theory for the initiation and propagation of radial hydraulic fractures in low-permeability materials. J. Geophys. Res.Solid Earth 122, 1239–1263.

Lee, K.K., Ellsworth, W.L., Giardini, D., Townend, J., Ge, S., Shimamoto, T., Yeo, I.W., Kang, T.S., Rhie, J., Sheen, D.H., Chang, C., 2019. Managing injection-induced seismic risks. Science 364, 730–732.

Lei, X., Ma, S., 2014. Labortory acoustic emission study for earthquake generation process. Earthq. Sci. 27 (6), 627–646.

Lei, X., Kusunose, K., Rao, M.V.M.S., Mishizawa, O., Satoh, T., 2000. Quasi-static fault growth and cracking in homogeneous brittle rock under triaxial compression using acoustic emission monitoring. J. Geophys. Res. 105 (B3), 6127–6139.

Lei, X., Funatsu, T., Ma, S., Liu, L., 2016. A laboratory acoustic emission experiment and numerical simulation of rock fracture driven by a high-pressure fluid source. J. Rock Mech. Geotech. Eng. 8, 27–34.

Li, M., Zhang, F., Zhuang, L., Zhang, X., Ranjith, P., 2019. Micromechanical analysis of hydraulic fracturing in the toughness-dominated regime: implications to supercritical carbon dioxide fracturing. Comput. Geosci. https://doi.org/10.1007/ s10596-019-09925-5.

Li, N., Ma, X., Zhang, S., Zou, Y., Wu, S., Li, S., Zhang, Z., Cao, T., 2020a. Thermal effects on the physical and mechanical properties and fracture initiation of Laizhou granite during hydraulic fracturing. Rock Mech. Rock. Eng. 53, 2539–2556.

Li, Q., Xing, H., Liu, J., Liu, X., 2015. A review on hydraulic fracturing of unconventional reservoir. Petroleum 1, 8–15.

Li, X., Li, S., He, J., He, P., Shi, R., 2020b. In-situ computed tomography technique in geomechanical testing. In: da Fontoura, S., Rocca, R.J., Pav´on Mendoza, J. (Eds.), Rock Mechanics for Natural Resources and Infrastructure Development, Proceedings of the 14th International Congress on Rock Mechanics and Rock Engineering (ISRM 2019). CRC Press, pp. 80–102.

Lin, H., Kang, W.H., Oh, J., Canbulat, I., 2020a. Estimation of in situ maximum horizontal principal stress magnitudes from borehole breakout data using machine learning. Int. J. Rock Mech. Min. Sci. 126, 104199.

Lin, H., Oh, J., Canbulat, I., Stacey, T.R., 2020b. Experimental and analytical investigations of the effect of hole size on borehole breakout geometries for estimating in situ stresses. Rock Mech. Rock. Eng. 53, 781–798.

Liu, P., Ju, Y., Gao, F., Ranjith, P.G., Zhang, Q., 2018. CT identification and fractal characterization of 3-D propagation and distribution of hydrofracturing cracks in low-permeability heterogeneous rocks. J. Geophys. Res. Solid Earth 123, 2156–2173.

Lockner, D., 1993. The role of acoustic emission in the study of rock fracture. Int. J. Rock Mech. Min. Sci. Geomech. Abstr. 30 (7), 883–899.

Lockner, D., Byerlee, J.D., 1977. Hydrofracture in Weber sandstone at high confining pressure and differential stress. J. Geophys. Res. 82 (14), 2018–2026.

López-Comino, J.A., Cesca, S., Heimann, S., Grigoli, F., Milkereit, C., Dahm, T., Zang, A., 2017. Characterization of hydraulic fractures growth during the Äspö hard rock laboratory experiment (Sweden). Rock Mech. Rock. Eng. 50, 2985–3001.

Lu, G., Uwaifo, E.C., Ames, B.C., Ufondu, A., Bunger, A.P., Prioul, R., Aidagulov, G., 2015. Experimental demonstration of delayed initiation of hydraulic fractures below breakdown pressure in granite. In: The 49th US Rock Mechanics/Geomechanics Symposium, San Francisco, ARMA 2015-190.

Lu, G., Gordeliy, E., Prioul, R., Aidagulov, G., Uwaifo, E.C., Ou, Q., Bunger, A.P., 2020. Time-dependent hydraulic fracture initiation. J. Geophys. Res. Solid Earth 125 (3), e2019JB018797.

Majer, E.L., Baria, R., Stark, M., Oates, S., Bommer, J., Smith, B., Asanuma, H., 2007. Induced seismicity associated with enhanced geothermal systems. Geothermics 36 (3), 185–222.

Manthei, G., 2005. Characterization of acoustic emission sources in a rock salt specimen under triaxial compression. Bull. Seismol. Soc. Am. 95 (5), 1674–1700.

Manthei, G., 2017. Moment tensor evaluation of acoustic emission sources in rock. In: Feng, X. (Ed.), Rock Mechanics and Engineering, 4. CRC Press/Balkema, pp. 478–527.

Mao, R., Feng, Z., Liu, Z., Zhao, Y., 2017. Laboratory hydraulic fracturing test on large-scale pre-cracked granite specimens. J. Nat. Gas Sci. Eng. 44, 278–286.

Martin, C.D., Martino, J.B., Dzik, E.J., 1994. Comparison of borehole breakouts from laboratory and field tests. In: The SPE/ISRM Rock Mechanics in Petroleum Engineering, August 29-31, Delft. SPE 28050.

McClure, M.W., Horne, R.N., 2014. An investigation of stimulation mechanisms in enhanced geothermal systems. Int. J. Rock Mech. Min. Sci. 72, 242–260.

McLaskey, G.C., Kilgore, B.D., Lockner, D.A., Beeler, N.M., 2014. Laboratory generated M -6 earthquakes. Pure Appl. Geophys. 171, 2601–2615.

McLaskey, G.C., Lockner, D.A., Kilgore, B.D., Beeler, N.M., 2015. A robust calibration technique for acoustic emission systems based on momentum transfer from a ball drop. B. Seismol. Soc. Am. 105 (1), 257–271.

Medlin, W.L., Masse, L., 1976. Laboratory investigation of fracture initiation pressure and orientation. In: The SPE-AXME 51st Annual Fall Technical Conference and Exhibition, New Orleans, SPE 6087.

Meier, P.M., Rodríguez, A., Bethmann, F., 2015. Lessons learned from Basel: new EGS projects in Switzerland using multistage stimulation and a probabilistic traffic light system for the reduction of seismic risk. In: World Geothermal Congress 2015, April 19-25, Melbourne.

Morita, N., Black, A.D., Fuh, G.F., 1996. Borehole breakdown pressure with drilling fluids–I. Empirical results. Int. J. Rock Mech. Min. Sci. Geomech. Abstr. 33 (1), 39–51.

Niemz, P., Cesca, S., Heimann, S., Grigoli, F., von Specht, S., Hammer, C., Zang, A., Dahm, T., 2020. Full-waveform-based characterization of acoustic emission activity in a mine-scale experiment: a comparison of conventional and advanced hydraulic fracturing schemes. Geophys. J. Int. 222 (1), 189–206.

Nordgren, R.P., 1972. Propagation of a vertical hydraulic fracture. SPE J. 12 (4), 306–314. SPE-3009-PA. Ohtani, T., Nakashima, Y., Nakano, T., Muraoka, H., 2000. X-ray CT imaging of pores and fractures in the Kakkonda granite, NE Japan. In: World Geothermal Congress 2000, May 28 - June 10, Kyushu - Tohoku.

Ohtsu, M., Okamoto, T., Yuyama, S., 1998. Moment tensor analysis of acoustic emission for cracking mechanisms in concrete. ACI Struct. J. 95 (2), 87–95. Osborne, F.F., 1935. Rift, grain and hardway in some Precambrian granites, Quebec. Econ. Geol. 30, 540–551.

Osiptsov, A.A., 2017. Fluid mechanics of hydraulic fracturing: a review. J. Pet. Sci. Eng. 156, 513–535. Patel, S.M., Sondergeld, C.H., Rai, C.S., 2017. Laboratory studies of hydraulic fracturing by cyclic injection. Int. J. Rock Mech. Min. Sci. 95, 8–15.

Pater, C.J., Groenenboom, J., van Dam, D.B., Romijn, R., 2001. Active seismic monitoring of hydraulic fractures in laboratory experiments. Int.

J. Rock Mech. Min. Sci. 38, 777–785.
Peng, S., Johnson, A.M., 1972. Crack growth and faulting in cylindrical specimens of Chelmsford granite. Int. J. Rock Mech. Min. Sci. 9 (1), 37–86.
Perkins, T.K., Kern, L.R., 1961. Widths of hydraulic fractures. J. Pet. Technol. 13 (9), 937–949. SPE-89-PA.
Petružálek, M., Jechumtálová, Z., Šílený, J., Kolář, P., Svitek, T., Lokajíček, T., Turková, I., Kotrlý, M., Onysko, R., 2020. Application of the shear-tensile source model to acoustic emissions in Westerly granite. Int. J. Rock Mech. Min. Sci. 128 https://doi.org/10.1016/j.ijrmms.2020.104246.
Rathnaweera, T.D., Wu, W., Ji, Y., Gamage, R.P., 2020. Understanding injection-induced seismicity in enhanced geothermal systems: From the coupled thermo-hydro-mechanical-chemical process to anthropogenic earthquake prediction. Earth-Sci. Rev. 205, 103182.
Renard, F., Bernard, D., Desrues, J., Ougier-Simonin, A., 2009. 3D imaging of fracture propagation using synchrotron X-ray microtomography. Earth Planet. Sci. Lett. 286, 285–291.
RILEM Technical Committee, 2010. Recommendation of RILEM TC 212-ACD: acoustic emission and related NDE techniques for crack detection and damage evaluation in concrete: Test method for damage qualification of reinforced concrete beams by Acoustic Emission. Mater. Struct. 43, 1187–1189. https://doi.org/10.1617/s11527- 010-9640-6.
Rubin, M.B., 1983. Experimental study of hydraulic fracturing in an impermeable material. J. Energy Resour. Technol. 105, 116–124.
Rummel, F., 1987. Fracture mechanics approach to hydraulic fracturing stress measurements. In: Atkinson, B.K. (Ed.), Fracture Mechanics of Rock. Academic Press, pp. 217–239.
Rummel, F., Winter, R.B., 1983. Application of laboratory fracture mechanics data to hydraulic fracturing field tests. In: Nemat-Nasser, S., Ab´e, H., Hirakawa, S. (Eds.), Hydraulic Fracturing and Geothermal Energy. Mechanics of Elastic and Inelastic Solids, 5. Springer, Dordrecht.
Sammis, C.G., Ashby, M.F., 1986. The failure of brittle porous solids under compressive stress states. Acta Metall. 34 (3), 511–526.
Sampath, K.H.S.M., Perera, M.S.A., Ranjith, P.G., 2018. Theoretical overview of hydraulic fracturing break-down pressure. J. Nat. Gas Sci. Eng. 58, 251–265.
Sarmadivaleh, M., Rasouli, V., 2015. Test design and sample preparation procedure for experimental investigation of hydraulic fracturing interaction modes. Rock Mech. Rock. Eng. 48, 93–105.
Savanick, G.A., Johnson, D.I., 1974. Measurement of the strength of grain boundaries in rock. Int. J. Rock Mech. Min. Sci. Geomech. Abstr. 11, 173–180.
Schill, E., Genter, A., Guenot, N., Koh, T., 2017. Hydraulic performance history at the Soultz EGS reservoirs from stimulation and long-term circulation tests. Geothermics 70, 110–124.
Schmitt, D.R., Zoback, M.D., 1989. Poroelastic effects in the determination of the maximum horizontal principal stress in hydraulic fracturing tests–a proposed breakdown equation employing a modified effective stress relation for tensile failure. Int. J. Rock Mech. Min. Sci. Geomech. Abstr. 26, 499–506.
Schmitt, D.R., Zoback, M.D., 1992. Diminished pore pressure in low porosity crystalline rock under tensional failure: apparent strengthening by dilatancy. J. Geophys. Res. 97, 273–288.
Schmitt, D.R., Zoback, M.D., 1993. Infiltration effects in the tensile rupture of thin walled cylinders of glass and granite: implications for the hydraulic fracturing breakdown equation. Int. J. Rock Mech. Min. Sci. Geomech. Abstr. 30 (3), 289–303.
Schubnel, A., Thompson, B., Fortin, J., Guéguen, Y., Young, R., 2007. Fluid-induced rupture experiment on Fontainebleau sandstone: Premonitory activity, rupture propagation, and aftershocks. Geophys. Res. Lett. 34, L19307 https://doi.org/ 10.1029/2007GL031076.
Selvadurai, P., Selvadurai, P.A., Nejati, M., 2019. A multi-phasic approach for estimating the Biot coefficient for Grimsel granite. Solid Earth 10, 2001–2014.
Serata, S., Sakuma, S., Kikuchi, S., Mizuta, Y., 1992. Double fracture method of in-situ stress measurement in brittle rock. Rock Mech. Rock. Eng. 25, 89–108.
Shen, B., Guo, H., Ko, T.Y., et al., 2013. Coupling rock-fracture propagation with thermal stress and fluid flow. Int. J. Geomech. 13 (6), 794–808.
Shimizu, H., Murata, S., Ishida, T., 2011. The distinct element analysis for hydraulic fracturing with fluid having different viscosity and particle size distribution. Int. J. Rock Mech. Min. Sci. 48, 712–727.
Smart, B.G.D., 1995. A true triaxial cell for testing cylindrical rock specimens. Int. J. Rock Mech. Min. Sci. Geomech. Abstr. 32 (3), 269–275.
Solberg, P., Lockner, D., Byerlee, J.D., 1977. Shear and tension hydraulic fractures in low permeability rocks. Pure Appl. Geophys. 115 (1), 191–198.
Solberg, P., Lockner, D., Byerlee, J.D., 1980. Hydraulic fracturing in granite under geothermal conditions. Int. J. Rock Mech. Min. Sci. Geomech. Abstr. 17 (1), 25–33.
Stanchits, S., Vinciguerra, S., Dresen, G., 2006. Ultrasonic velocities, acoustic emission characteristics and crack damage of basalt and granite. Pure Appl. Geophys. 163, 974–993.
Stanchits, S., Mayr, S., Shapiro, S., Dresen, G., 2011. Fracturing of porous rock induced by fluid injection. Tectonophysics 503, 129–145.
Stanchits, S., Surdi, A., Edelman, E., Suarez-Rivera, R., 2012. Acoustic emission and ultrasonic transmission monitoring of hydraulic fracture initiation and growth in rock samples. In: The 30th European Conference on Acoustic Emission Testing & 7th International Conference on Acoustic Emission, Granada, Spain.
Stephansson, O., Semikova, H., Zimmermann, G., Zang, A., 2019. Laboratory pulse test of hydraulic fracturing on granitic sample cores from Äspö HRL, Sweden. Rock Mech. Rock. Eng. 52, 629–633.
Stephens, G., Voight, B., 1982. Hydraulic fracturing theory for conditions of thermal stress. J. Rock Mech. Min. Sci. & Geotech. Abstr. 19, 279–284.
Stoeckhert, F., Molenda, M., Brenne, S., Alber, M., 2015. Fracture propagation in sandstone and slate – Laboratory experiments, acoustic emissions and fracture mechanics. J. Rock Mech. Geotech. Eng. 7, 237–249.
Suckale, J., 2009. Induced seismicity in hydrocarbon fields. In: Renata Dmowska (ed). Adv. Geophys. 51, 55–106. Takehara, T., Soma, N., Tosha, T., Yamaguchi, T., 2003. Experimental study on artificial fracture opening behavior by laboratory hydraulic fracturing test. In: Rock Stress, Sugawara, Obara, Sato (Eds.), Rock Stress '03: Proceedings of the Second International Symposium on Rock Stress. November 4-6, Kumamoto.
Thomas, N., Weijermars, R., 2018. Comprehensive atlas of stress trajectory patterns and stress magnitudes around cylindrical holes in rock bodies for geoscientific and geotechnical applications. Earth-Sci. Rev. 179, 303–4371.
Veatch Jr., R.W., Moschovidis, Z.A., 1986. An overview of recent advances in hydraulic fracturing technology. Soc. Pet. Eng. J. l26, 421–454.
Waldhauser, F., Ellsworth, W.L., 2000. A double-difference earthquake location algorithm: method and Application to the Northern Hayward fault, California. Bull. Seismol. Soc. Am. 90 (6), 1353–1368.
Wang, Y., Zhang, D., Hu, Y.Z., 2019a. Laboratory investigation of the effect of injection rate on hydraulic fracturing performance in artificial transversely laminated rock using 3D laser scanning. Geotech. Geol. Eng. 37, 2121–2133.
Wang, Y., Teng, Q., He, X., Feng, J., Zhang, T., 2019b. CT-image of rock samples super resolution using 3D convolutional neural network. Comput. Geosci. 133, 104314. https://doi.org/10.1016/j.cageo.2019.104314.
Warpinski, N.R., Du, J., Zimmer, U., 2012. Measurements of hydraulic-fracture-induced seismicity in gas shales. In: SPE Hydraulic Fracturing Technology Conference, Woodlands, February 6-8, Article ID: 151597.
Watanabe, N., Egawa, M., Sakaguchi, K., Ishibashi, T., Tsuchiya, N., 2017a. Hydraulic fracturing and permeability enhancement in granite from subcritical/brittle to supercritical/ductile conditions. Geophys. Res. Lett. 44, 5468–5475.
Watanabe, N., Numakura, T., Sakaguchi, K., Saishu, H., Okamoto, A., Ingebritsen, S.E., Tsuchiya, N., 2017b. Potentially exploitable supercritical geothermal resources in the ductile crust. Nat. Geosci. 10, 140–144.
Watanabe, N., Sakaguchi, K., Goto, R., Miura, T., Yamane, K., Ishibashi, T., Chen, Y., Komai, T., Tsuchiya, N., 2019. Cloud-fracture networks as a means of accessing superhot geothermal energy. Sci. Rep. 9, 939. https://doi.org/10.1038/s41598-018- 37634-z.
Weijers, L., de Pater, C.J., Owens, K.A., Kogsbøll, H.H., 1994. Geometry of hydraulic fractures induced from horizontal wellbores. Soc. Petrol. Engrs. https://doi.org/ 10.2118/25049-PA.
Wu, F., Li, D., Fan, X., Liu, J., Li, X., 2020. Analytical interpretation of

hydraulic fracturing initiation pressure and breakdown pressure. J. Nat. Gas Sci. Eng. 76, 103185.
Xie, L., Min, K.B., Song, Y., 2015. Observations of hydraulic stimulations in seven enhanced geothermal system projects. Renew. Energy 79, 56–65.
Xing, Y., Zhang, G., Luo, T., Jiang, Y., Ning, S., 2019. Hydraulic fracturing in high-temperature granite characterized by acoustic emission. J. Pet. Sci. Eng. 178, 475–484.
Xiong, Q., Lin, Q., Hampton, J.C., 2021. Temporal evolution of a shear-type rock fracture process zone (FPZ) along continuous, sequential, and spontaneously well-separated laboratory instabilities—from intact rock to thick gouged fault. Geophys. J. Int., ggab041 https://doi.org/10.1093/gji/ggab041.
Yamamoto, K., Naoi, M., Chen, Y., Nishihara, K., Yano, S., Kawakata, H., Akai, T., Kurosawa, I., Ishida, T., 2019. Moment tensor analysis of acoustic emissions induced by laboratory-based hydraulic fracturing in granite. Geophys. J. Int. 216, 1507–1516.
Ye, Z., Ghassemi, A., 2018. Injection-induced shear slip and permeability enhancement in granite fractures. J. Geophys. Res. Solid Earth 123, 9009–9032.
Ye, Z., Ghassemi, A., 2019. Injection-induced propagation and coalescence of preexisting fractures in granite under triaxial stress. J. Geophys. Res. Solid Earth 124, 7806–7821.
Yew, C.H., Weng, X., 2015. Mechanics of hydraulic fracturing (Second Edition). Gulf Professional Publishing, p. 234.
Yin, T., Li, X., Cao, W., Xia, K., 2015. Effects of thermal treatment on tensile strength of Laurentian granite using Brazilian test. Rock Mech. Rock. Eng. 48, 2213–2223.
Yoon, J.S., Zang, A., Stephansson, O., 2014. Numerical investigation on optimized stimulation of intact and naturally fractured deep geothermal reservoirs using hydro-mechanical coupled discrete particles joints model. Geothermics 52, 165–184.
Yoon, J.S., Zimmermann, G., Zang, A., 2015a. Discrete element modeling of cyclic rate fluid injection at multiple locations in naturally fractured reservoirs. Int. J. Rock Mech. Min. Sci. 74, 15–23.
Yoon, J.S., Zimmermann, G., Zang, A., 2015b. Numerical investigation on stress shadowing in fluid injection-induced fracture propagation in naturally fractured geothermal reservoirs. Rock Mech. Rock. Eng. 48 (4), 1439–1454.
Zang, A., Stephansson, O., 2010. Stress field of the earth's crust. Springer.
Zang, A., Stephasson, O., 2019. Special issue "Hydraulic fracturing in hard rock". Rock Mech. Rock. Eng. 52, 471–473.
Zang, A., Wagner, F., Dresen, G., 1996. Acoustic emission, microstructure, and damage model of dry and wet sandstone stressed to failure. J. Geophys. Res. 101(B8), 17507–17521.
Zang, A., Wagner, F.C., Stanchits, S., Dresen, G., Andresen, R., Haidekker, M., 1998. Source analysis of acoustic emissions in Aue granite cores under symmetric and asymmetric compressive loads. Geophys. J. Int. 135, 1113–1130.
Zang, A., Wagner, F.C., Stanchits, S., Janssen, C., Dresen, G., 2000. Fracture process zone in granite. J. Geophys. Res. Solid Earth 105 (B10), 23651–23661.
Zang, A., Stanchits, S., Dresen, G., 2002. Acoustic emission controlled triaxial rock fracture and friction tests. In: Dyskin, A.V., Hu, X., Sahouryeh, E. (Eds.), Structural integrity and fracture. Swets & Zeitlinger, Lisse, pp. 289–294.
Zang, A., Yoon, J.S., Stephansson, O., Heidbach, O., 2013. Fatigue hydraulic fracturing by cyclic reservoir treatment enhances permeability and reduces induced seismicity. Geophys. J. Int. 195 (2), 1282–1287.
Zang, A., Oye, V., Jousset, P., Deichmann, N., Gritto, R., McGarr, A., Majer, E., Bruhn, D., 2014. Analysis of induced seismicity in geothermal reservoirs – An overview. Geothermics 52, 6–21.
Zang, A., Stephansson, O., Stenberg, L., Plenkers, K., Specht, S., Milkereit, C., Schill, E., Kwiatek, G., Dresen, G., Zimmermann, G., Dahm, T., Weber, M., 2017. Hydraulic fracture monitoring in hard rock at 410 m depth with an advanced fluid-injection protocol and extensive sensor array. Geophys. J. Int. 208 (2), 790–813.
Zang, A., Zimmermann, G., Hofmann, H., Stephansson, O., Min, K.B., Kim, K.Y., 2019. How to reduce fluid-injection-induced seismicity. Rock Mech. Rock. Eng. 52, 475–493. https://doi.org/10.1007/s00603-018-1467-4.
Zhang, F., Damjanac, B., Maxwell, S., 2019b. Investigating hydraulic fracturing complexity in naturally fractured rock masses using fully coupled multiscale numerical modeling. Rock Mech. Rock. Eng. 52, 5137–5160.
Zhang, W., Guo, T., Qu, Z., Wang, Z., 2019a. Research of fracture initiation and propagation in HDR fracturing under thermal stress from meso-damage perspective. Energy 178, 508–521.
Zhao, Z., Kim, H., Haimson, B., 1996. Hydraulic fracturing initiation in granite. In: Aubertin, Hassani, Mitri (Eds.), Rock Mechanics. Balkema, Rotterdam, pp. 1279–1284. Zhou, C., Wan, Z., Zhang, Y., Gu, B., 2018. Experimental study on hydraulic fracturing of granite under thermal shock. Geothermics 71, 146–155.
Zhou, J., Jin, Y., Chen, M., 2010. Experimental investigation of hydraulic fracturing in random naturally fractured blocks. Int. J. Rock Mech. Min. Sci. 47, 1193–1199.
Zhou, Z., Jin, Y., Zeng, Y., Zhang, X., Zhou, J., Zhuang, L., Xin, S., 2020. Investigation on fracture creation in hot dry rock geothermal formations of China during hydraulic fracturing. Renew. Energy 153, 301–313.
Zhuang, L., Diaz, M., Jung, S.G., Kim, K.Y., 2016. Cleavage dependent indirect tensile strength of Pocheon granite based on experiments and DEM simulation. Tunn. Undergr. Sp. KSCE 26 (4), 316–326.
Zhuang, L., Kim, K.Y., Jung, S.G., Diaz, M., Min, K.B., Park, S., Zang, A., Stephansson, O., Zimmermann, G., Yoon, J.S., 2018a. Cyclic hydraulic fracturing of cubic granite samples under triaxial stress state with acoustic emission, injectivity and fracture measurements. In: The 52nd US Rock Mechanics/Geomechanics Symposium. Seattle, ARMA 18–297.
Zhuang, L., Kim, K.Y., Yeom, S., Jung, S.G., Diaz, M., 2018b. Preliminary laboratory study on initiation and propagation of hydraulic fractures in granite using X-ray Computed Tomography. In: International Conference on Geomechanics, Geo-energy and Geo-resources (IC3G2018), Sep 22-24, Chengdu.
Zhuang, L., Kim, K.Y., Shin, H.S., Jung, S.G., Diaz, M., 2018c. Experimental investigation of effects of borehole size and pressurization rate on hydraulic fracturing breakdown pressure of granite. In: The 10th Asian Rock Mechanics Symposium, Oct 29 - Nov 3, Singapore.
Zhuang, L., Kim, K.Y., Jung, S.G., Diaz, M., Min, K.B., 2019a. Effect of water infiltration, injection rate and anisotropy on hydraulic fracturing behavior of granite. Rock Mech. Rock. Eng. 52, 575–589.
Zhuang, L., Kim, K.Y., Jung, S.G., Diaz, M., Min, K.B., Zang, A., Stephansson, O., Zimmermann, G., Yoon, J.S., Hofmann, H., 2019b. Cyclic hydraulic fracturing of pocheon granite cores and its impact on breakdown pressure, acoustic emission amplitudes and injectivity. Int. J. Rock Mech. Min. Sci. 122 https://doi.org/ 10.1016/j.ijrmms.2019.104065.
Zhuang, L., Kim, K.Y., Diaz, M., Yeom, S., 2020a. Evaluation of water saturation effect on mechanical properties and hydraulic fracturing behavior of granite. Int. J. Rock Mech. Min. Sci. 130 https://doi.org/10.1016/j.ijrmms.2020.104321.
Zhuang, L., Jung, S.G., Diaz, M., Kim, K.Y., 2020b. Laboratory investigation on hydraulic fracturing of granite core specimens. In: Shen, B., Stephansson, O., Rinne, M. (Eds.), Modelling Rock Fracturing Processes–Theories, Methods, and Applications. Springer Nature Switzerland AG.
Zhuang, L., Kim, K.Y., Jung, S.G., Diaz, M., Hofmann, H., Min, K.B., Zang, A., Zimmermann, G., Stephansson, O., Yoon, J.S., 2020c. Laboratory true triaxial hydraulic fracturing of granite under six fluid injection schemes and grain-scale fracture observations. Rock Mech. Rock. Eng. 53, 4329–4344.
Zhuang, L., Yeom, S., Pham Ngoc, C., Sun, C., Jung, S.G., Shin, H.S., 2020d. Experimental investigation of permeability and fracture aperture variations with confining pressure through in-situ X-ray CT. In: International Conference on Coupled Processes in Fractured Geological Media: Observation, Modleing, and Application, Nov 11-13, Seoul.
Zimmermann, G., Moeck, I., Blöcher, G., 2010. Cyclic waterfrac stimulation to develop an Enhanced Geothermal System (EGS) – Conceptual design and experimental results. Geothermics 39 (1), 59–69.
Zimmermann, G., Zang, A., Stephansson, O., Klee, G., Semikov´a, H., 2019. Permeability enhancement and fracture development of hydraulic in situ experiments in the Äspö Hard Rock Laboratory. Sweden. Rock Mech. Rock Eng. 52, 495–515.
Zoback, M.D., 2007. Reservoir Geomechanics. Cambridge University Press, Cambridge. https://doi.org/10.1017/CBO9780511586477.
Zoback, M.D., Byerlee, J.D., 1975. The effect of microcrack dilatancy on the permeability of Westerly granite. J. Geophys. Res. 80, 752–755. Zoback, M.D., Gorelick, S.M., 2012. Earthquake triggering and large-scale

geologic storage of carbon dioxide. Proc. Natl. Acad. Sci. 109 (26), 10164–10168.
Zoback, M.D., Rummel, F., Jung, R., Raleigh, C.B., 1977. Laboratory hydraulic fracturing experiments in intact and pre-fractured rock. Int. J. Rock Mech. Min. Sci. Geomech. Abstr. 14, 49–58.
Zou, Y., Zhang, S., Zhou, T., Zhou, X., Guo, T., 2016. Experimental investigation into hydraulic fracture network propagation in gas shales using CT scanning technology. Rock Mech Rock Eng 49, 33–45.